Characterizing Unsteadiness in Supersonic Retropropulsion Flows

Brenton W. Ho

A thesis
submitted in partial fulfillment of the
requirements for the degree of

MASTER OF SCIENCE IN AERONAUTICS & ASTRONAUTICS

University of Washington

2019

Reading Committee:

Owen Williams, Chair

Carl Knowlen

Program Authorized to Offer Degree:
Aeronautics & Astronautics

University of Washington

Abstract

Characterizing Unsteadiness in Supersonic Retropropulsion Flows

Brenton W. Ho

Chair of the Supervisory Committee:
Dr. Owen Williams
Aeronautics & Astronautics

Supersonic retropropulsion (SRP) is an increasingly important entry, descent, and landing technology with applications to both planetary exploration and commercial spaceflight. Unsteadiness, and the conditions under which it appears, in SRP flows is poorly understood. Improved predictive models of SRP flow phenomena will lead to more efficient and effective use of the technology. This thesis studies the effect of forebody size on SRP flowfield phenomena using high-speed schlieren imagery. A series of retronozzles and forebodies were tested over a range of stagnation pressure ratios in order to explore the conditions under which SRP flow unsteadiness occurs and the modes of unsteadiness found under these conditions. An analysis method was developed which effectively stabilizes unwanted retronozzle motion, identifies and tracks the shock fronts, and extracts frequency spectra for unsteady motion. Mean and RMS images for each test case were also examined to highlight flow structure and regions of unsteadiness. For each of these cases, one of two types of unsteadiness were observed: bow shock oscillation or bow shock rippling/penetration. The appearance of one or the other was found to be dependent on forebody size and jet pressure. Significantly, frequencies of bow shock motion and Strouhal numbers of $\mathcal{O}(10^{-1})$ were extracted for each unsteady case and found to point to the possibility of a single underlying mechanism which may drive SRP unsteadiness.

TABLE OF CONTENTS

LIST OF FIGURES

LIST OF TABLES

NOMENCLATURE

β: ballistic coefficient

M: mass

C_D: coefficient of drag

C_T: coefficient of thrust

C_A: total force coefficient

A: area

P: pressure

f: frequency

D: diameter

U: velocity

T: thrust

St: Strouhal number

M_a: Mach number

A_j: nozzle exit area

A_{FB}: vehicle forebody reference area

Superscripts & Subscripts

$(\bullet)_0$: stagnation value

$(\bullet)_{jet}$: retrojet value

$(\bullet)_\infty$: freestream value

$(\bullet)_{amb}$: ambient value

ACKNOWLEDGMENTS

The author wishes to thank Dr. Owen Williams for his constant support and encouragement. Without his patience and mentorship this thesis would never have even gotten close to being written. The author also wishes to express gratitude to Charlie Yang for his boundless cheerfulness and genuine love for all things aerospace. Thanks are also in order for all of the support provided by close friends and family. Mom, Dad, Julaine, and Elliott, I truly couldn't have done it without you.

DEDICATION

To my constant partner, source of joy, and love of my life, Flannery.

Chapter 1
INTRODUCTION

With the shift from robotic to crewed missions to Mars on the horizon for NASA, the technological area of entry, descent, and landing (EDL) becomes increasingly important. NASA's 2015 Technology Roadmap for EDL notes that deceleration of an entry vehicle through aerodynamical drag alone limits the payload mass to a handful of tons [1]. Compared to previous missions to Mars, a human mission requires a significant increase in the delivered payload which in turn increases the ballistic coefficient, β, of the entry vehicle. Ballistic coefficient is a measure of the effectiveness of aerodynamic drag for slowing a vehicle upon atmospheric entry, it is defined below in Eq. 1.1.

$$\beta = \frac{m}{C_D A} \tag{1.1}$$

This increase in the ballistic coefficient means that greater effort is required to slow the entry vehicle. This is made even more challenging the low density of Mars' atmosphere which significantly lowers the effectiveness of drogue parachutes. This is highlighted by Figure 1.1, which depicts real and modeled landing trajectories for spacecraft entering the Martian atmosphere. The parts of the trajectory which fall outside of the yellow highlighted area are the high-energy phase of EDL. During this pahse, the entry vehicle is travelling at supersonic speeds at high altitudes. Typically, the only decelerative force the entry vehicles experience in this regime is the aerodynamic drag associated with the shape and size of the craft. The portion of the trajectories inside the yellow box is the low-energy phase of Mars EDL. This region corresponds to entry vehicles which have slowed down enough to employ traditional

landing methods such as drogue chutes and subsonic retropropulsion. As can be seen in the figure, a crewed landing vehicle based on the Apollo capsule would reach the martian surface traveling at over a kilometer per second under aerodynamic drag alone; much too fast for conventional landing technologies. These factors mean a potential crewed Mars mission would require alternative, supersonic methods of slowing the entry vehicle during descent and landing. NASA's low-density supersonic decelerator program demonstrated that drogue parachutes have difficulties deploying properly at supersonic velocities, further emphasizing the need for EDL technologies that slow the vehicle more significantly in the high-energy, high-speed portion of its flight [2].

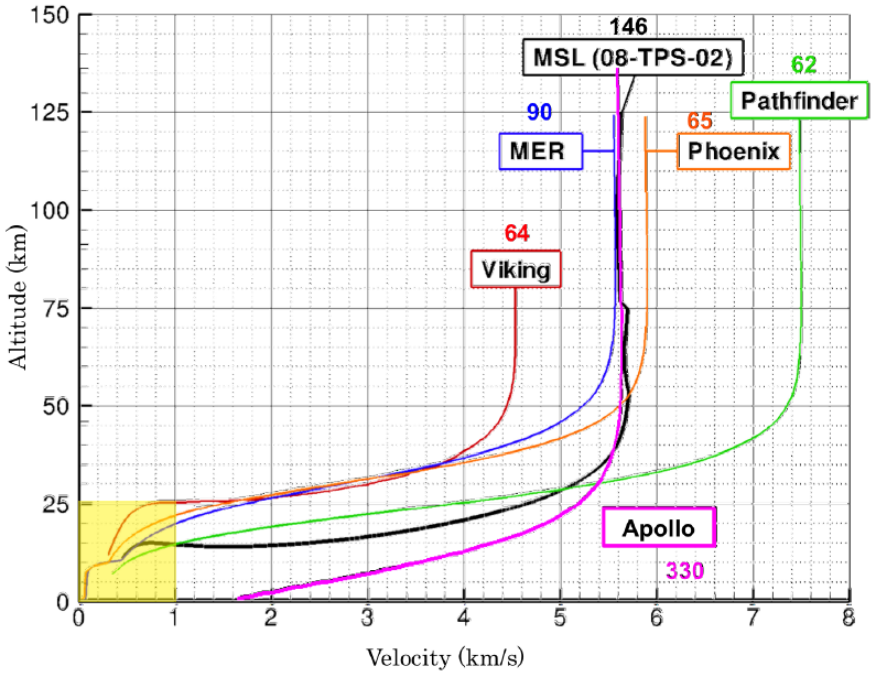

Figure 1.1: Trajectories of Mars surface missions showing velocity and altitude with the modeled Apollo trajectory in pink. The yellow region highlights the typical flight envelope for subsonic EDL methods. Ballistic coefficients are listed next to mission names. [3]

One promising EDL concept employs supersonic retropropulsion (SRP) to slow the entry

vehicle. SRP works by firing an engine into an oncoming supersonic or hypersonic flow, essentially thrusting in reverse. Utilization of SRP in a vehicle corresponds to an effective increase in C_D which in turn lowers ballistic coefficient. The idea is that one would be able to shift a Martian-entry vehicle far enough to the left in the chart in Figure 1.1 that the vehicle would exit the high-energy flow regime well above ground and re-enable the use of more classical powered and un-powered landing methods. SRP has the advantage that it is relatively simple, scalable to payload size, reusable, and it allows for greater control over landing trajectory when compared to passive methods. In addition, the SRP hardware can be reused for propulsive landing, eliminating the need for other methods of slowing the vehicle in terminal descent. The use of SRP is still in its infancy and the ability to predict its flow characteristics is important to further development of this technology. SRP flow dynamics are predicated upon many disparate phenomena including compressibility, heat transfer, and turbulence. Thus, the flow field surrounding the exit nozzle of an SRP system tends to be complex, with a number of known regimes of unsteadiness. Unsteadiness in the flow is generally undesirable as dynamic loading can have negative effects on the vehicle structure and can render control schemes inefficient if not properly understood. The dynamics of this unsteadiness are poorly understood at least in part due to the difficulty of SRP experimentation in general and also due to the fact that SRP unsteadiness itself is affected by many different flow and geometric parameters.

A series of studies have examined the influence of jet pressure on SRP flow structure. Many of these studies have looked at how stagnation pressure ratio, which is an SRP flow parameter closely related to coefficient of thrust, affects SRP flow structure. These studies have found that certain regimes of coefficient of thrust and stagnation pressure ratio result in penetration of the bow shock by the jet, a configuration which is unsteady [4–7]. Bow shock penetration is a disturbance in the topography of a previously smooth bow shock wherein a new structure emerges which has separate curvature and inflection points where it departs from the original shock front. These features can be seen in Figure 1.2 below. The prominence of this penetration can vary. Daso, et al. suggest that forebody size is

coupled with the appearance and prominence of bow shock penetration [7]. More recently, Tan identified a new regime of SRP bow shock unsteadiness which exhibits no penetration of the bow shock for a retronozzle with very little forebody area. Further, the bow shock moved forward and backward in as one coherent structure, with no obvious rippling or distortion [8]. This suggests the existence of two distinct types of SRP unsteadiness.

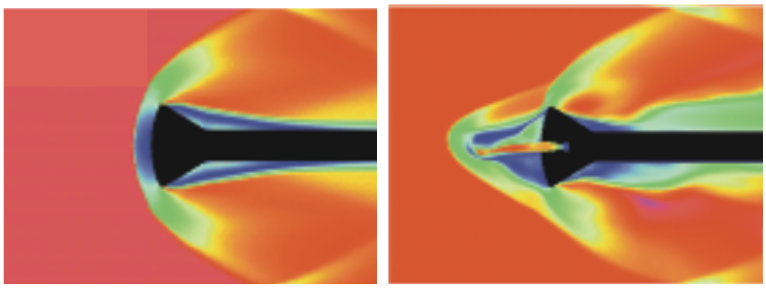

(a) (b)

Figure 1.2: (a) Bow shock with no penetration. (b) Bow shock with penetration.

These previous results raise the following questions, which this thesis will aim to address:

- How are the two types of known unsteadiness regimes related?
- How does jet-to-forebody diameter ratio affect transition from non-penetrating to penetrating unsteadiness?
- What are the frequencies associated with each type of unsteady regime?

This study utilizes schlieren high-speed video collected with a range of forebody sizes over a range of jet pressures to further characterize the unsteady regimes of SRP flowfields. Further, the effects of flow confinement and forebody size are investigated. Code was developed which effectively stabilizes unwanted retronozzle motion, identifies and tracks the shock fronts, and extracts frequency spectra for unsteady motion in each case. Mean and

RMS images for each test case were developed to highlight flow structure and regions of unsteadiness. It was determined that there are indeed two different modes of unsteadiness for the conditions tested here. The appearance of one mode or the other depended on the proportion of forebody relative to jet size in the retronozzle configuration. Frequencies of motion were extracted for each of the unsteady cases which point to the possibility of a single mechanism driving unsteadiness.

Chapter 2

BACKGROUND AND THEORY

2.1 Supersonic Retropropulsion

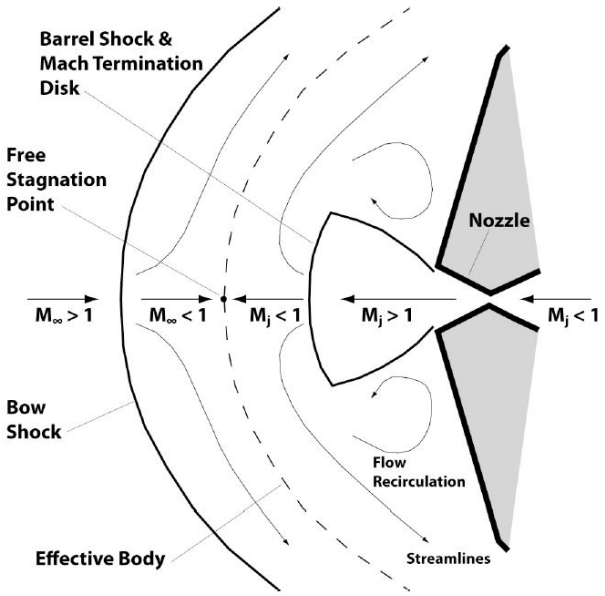

Figure 2.1: Basic sketch of SRP flow features. [5]

Figure 2.1 shows a sketch of the flow field for SRP with a centrally located retronozzle producing a highly underexpanded jet, which depicts the important features common to many SRP flow configurations. The freestream flow approaches at a supersonic velocity from the left and meets the bow shock (which is represented by the solid, thick black line in the sketch) where it is shocked down to subsonic speeds. The retrojet exits the nozzle from the right at a supersonic velocity and is also shocked down to a subsonic regime. The two subsonic flows meet and a stagnation point is formed where the velocity is zero relative to

the vehicle. The streamlines for the two flows follow the contact surface, which is represented by the dashed line in the sketch. Regions of recirculation can exist near the surface of the forebody in the immediate vicinity of the retronozzle exit. Recirculation is heavily influenced by the size of the forebody relative to the retrojet. The size of the forebody also has an influence on the base pressure of the forebody which is one of the primary determinants of the retrojet expansion pattern.

The exact behavior of the flow interaction, particularly for more complicated SRP configurations, and how it is affected by changes in the freestream and retrojet flow conditions is not well defined. The example discussed above is for a highly under-expanded jet. The features of the flow are highly dependent on retrojet pressure, a topic which is discussed more in the next section.

2.1.1 Theory

A common parameter of interest for SRP flows is the coefficient of thrust, C_T, which is defined in Eq. 2.1 below. C_T is a measure of the strength of the retrojet flow relative to freestream dynamic pressure in an SRP configuration. Another important parameter when considering SRP is the drag coefficient, C_D, which captures the aerodynamic drag contribution of the vehicle geometry to the total force coefficient, C_A, which is the sum total of C_T and C_D. The drag coefficient is defined in Eq. 2.2.

$$C_T = \frac{T}{q_\infty A_{fb}} \tag{2.1}$$

$$C_D = \frac{D}{q_\infty A_{fb}} \tag{2.2}$$

In the above equations, T is the thrust force produced by the retrojet, D is total aerodynamic drag produced by the body, q_∞ is the freestream dynamic pressure, and A_{fb} is the projected frontal area of the retropropulsing body. Since both of these quantities have an effect on the

trajectory of an entry vehicle entering the atmosphere, and indeed have an effect on each other, it is convenient to combine them into a total force coefficient when considering SRP. It should be noted that C_A is not simply a superposition of the C_D value of the vehicle with no jet and the C_T of the vehicle with the retrojet engaged. These values are coupled and their relationship is dependent on the retronozzle configuration.

For a centrally located retronozzle configuration, such as that shown in Figure 2.4, the coefficient of drag has been shown to decrease as coefficient of thrust is increased [9]. Figure 2.2 demonstrates that C_D drops to approximately 10% of it's no-jet value as C_T rises. Despite this reduction in C_D, however, the total force coefficient increases as C_T increases. The fraction of the total force on the vehicle produced by drag can be thought of as a measure of SRP efficiency. A common goal for improving SRP performance is to attempt to maintain the aerodynamic drag as much as possible while enhancing the total force with jet thrust.

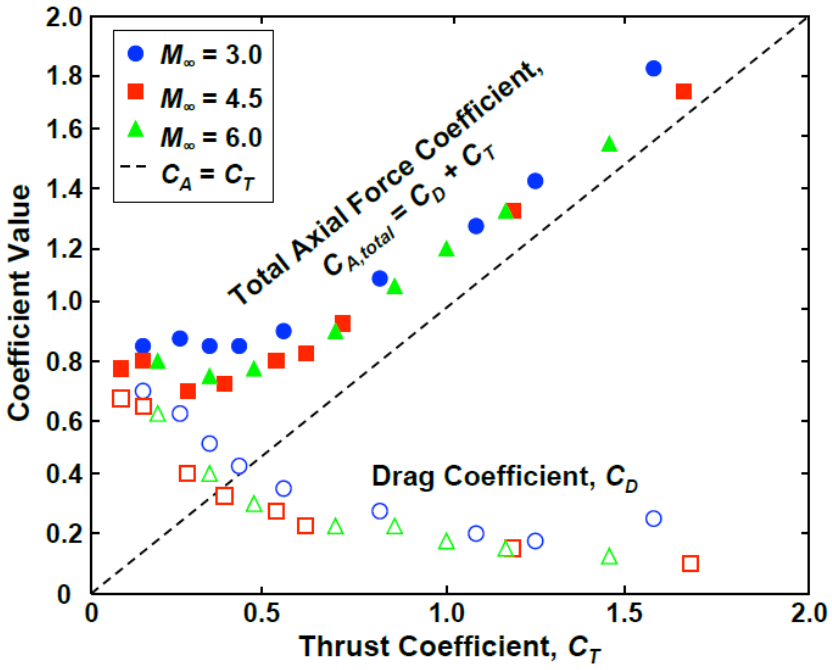

Figure 2.2: Variation of drag coefficient for increasing thrust coefficient in a central nozzle configuration SRP flow. Taken from Korzun [10] who adapted the figure from McGhee [9].

Coefficient of thrust, and thus the nature of the SRP flow, is closely dependent on the ratio of jet and freestream pressures as suggested by the earlier discussion of jet expansion patterns. For convenience, the ratio of jet and freestream stagnation pressures ($P_{0,jet}/P_{0,\infty}$) is often examined. The retronozzle jet area to forebody area ratio (A_j/A_{FB}), the nozzle geometry, the operating environment (Mach numbers, temperatures, and fluid densities), and propulsion fluid choice all also have effects on the flow field. This relationship is shown explicitly by Korzun [10] in Eq. 2.3 which is an equivalent expression of Eq. 2.1.

$$C_T = \frac{2(1+\gamma_{jet}Ma_{jet})}{\gamma_\infty Ma_\infty}\cdot\boxed{\frac{A_j}{A_{FB}}}\cdot(1+\frac{\gamma_{jet}-1}{2}Ma_{jet})^{-\frac{\gamma_{jet}}{\gamma_{jet}-1}}\cdot(1+\frac{\gamma_\infty-1}{2}Ma_\infty)^{-\frac{\gamma_\infty}{\gamma_\infty-1}}\cdot\boxed{\frac{P_{0,jet}}{P_{0,\infty}}} \quad (2.3)$$

While nozzle geometry and the gas properties of the retrojet have an influence on the SRP flow field, these properties are held constant in this study in order to highlight the effect of stagnation pressure ratio jet-to-forebody area ratio on flow field structure and behavior [11]. Additionally, the operating environment (i.e. the freestream Mach numbers and temperatures) is kept constant. Holding these parameters constant leaves only $P_{0,jet}/P_{0,\infty}$ and A_j/A_{FB} as independent variables to be investigated individually.

2.1.2 Retronozzle Flow

The pressure of the retrojet is one of the primary determinents of the structure and behavior of the SRP flow field. Thus, it is important to discuss the the structure and behavior of jets in various pressure regimes when exhausting into quiescent air. Retronozzle flows can be under-expanded, over-expanded, or perfectly expanded depending on the pressure difference between the jet exit plane and the ambient pressure of the surroundings. The flow conditions at the nozzle exit are determined by the stagnation pressure of the fluid passing through the retronozzle, the throat-to-exit area ratio, and the ambient conditions into which the retrojet is evacuating. It should be noted that for SRP flows, the ambient pressure value at the retronozzle exit is heavily influenced by the shape and size of the vehicle forebody. The

freestream flow properties and Mach number also determine the ambient pressure at the nozzle exit plane. Perfectly expanded jet flows are the simplest case in that the jet flow at the nozzle exits at the same pressure as the ambient conditions and therefore creates a straight shear layer and there is no turning of the flow at the exit.

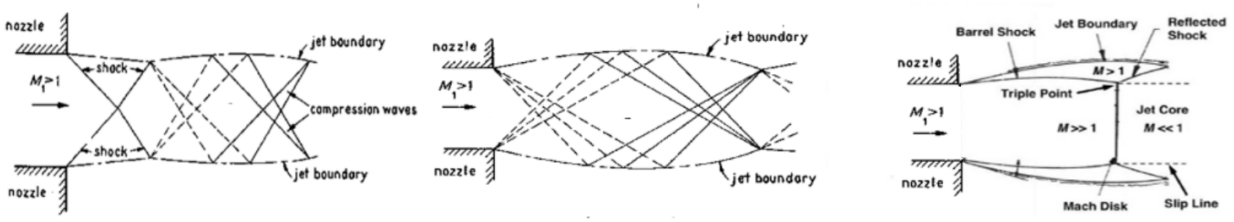

Figure 2.3: (left) over-expanded retronozzle flow field (center) under-expanded retronozzle flow field (right) highly under-expanded retronozzle flow field. Adapted from [12, 13]

Over-expanded jets occur when the exit pressure is less than the ambient ($P_{jet} < P_{amb}$). This negative pressure difference combined with the supersonic speed of the jet flow results in oblique shocks which compress and turn the flow toward the nozzle center-line. Another set of oblique shocks then have to turn the flow to be parallel to the center-line. The jet static pressure is then higher than the ambient pressure and subsequently the flow must expand and turn through a series of expansion waves. The jet flow is then compressed again by the waves reflected off of the jet boundary. This pattern continues until the flow pressure and the ambient pressure match and viscous effects eventually disperse the jet structure. The structural differences between under-expanded and over-expanded jets can be seen in Figure 2.3.

A similar pattern of flow turning and pressure matching occurs for slightly under-expanded jets. These occur when the exit pressure of the jet is greater than that of the quiescent fluid the nozzle is exhausting into ($P_{jet} > P_{amb}$). For a slightly under-expanded jet the flow must be expanded in order to lower the static pressure of the jet to meet the ambient value, this is accomplished through a series of expansion and compression waves.

Cases where the jet static pressure at the exit is much greater than the ambient ($P_{jet} >> P_{amb}$) are said to be highly under-expanded. For these cases, the pressure gradient is large enough to necessitate a significant Prandtl-Meyer expansion fan at the nozzle exit leading to a normal shock at some point downstream of the nozzle exit which is known as a Mach disk. The flow further downstream from the Mach disk is subsonic. The radial flow is shocked down with a curved bulging structure known as a barrel shock and again through a reflected shock coming from the Mach disk-barrel shock intersection, this turns flow back towards the axial direction while still keeping it supersonic. An interesting feature of this type of jet is that downstream of the mach disk, the subsonic core jet is encased in a sleeve of supersonic flow.

2.1.3 Unsteadiness & Bow Shock Penetration

Moving from the over-expanded, through slightly under-expanded to greatly under-expanded, there is a trend of increasing momentum carried downstream of the jet exit. This increased energy contribution to the flow has significant effects on the structure of an SRP flow field. Stagnation pressure ratios corresponding to these regimes are tested for this thesis.

Many previous SRP studies have observed steady flow at flow for low and high thrust regimes but unsteady flow at some intermediate retrojet pressure or thrust [7] [14] [4]. It has been shown that, for SRP configurations with a retronozzle located centrally within an axially symmetric forebody, there exist flow regimes which exhibit dynamic behavior. Romeo & Sterrett [4] found that a jet with large enough mass flux facing a supersonic freestream would create a bulge in the bow shock. Berry et al. [5,6] found that multi-nozzle configurations and non-axial freestream flow caused bow shock unsteadiness as well. Daso et al. [7] found that varying the stagnation pressure ratio resulted in the retrojet penetrating the bow shock for their retronozzle configuration at $P_{0,jet}/P_{0,\infty}$ values of approximately one or two. This phenomenon can be seen for both numerical models and experimental results in Figures 2.4 & 2.5.

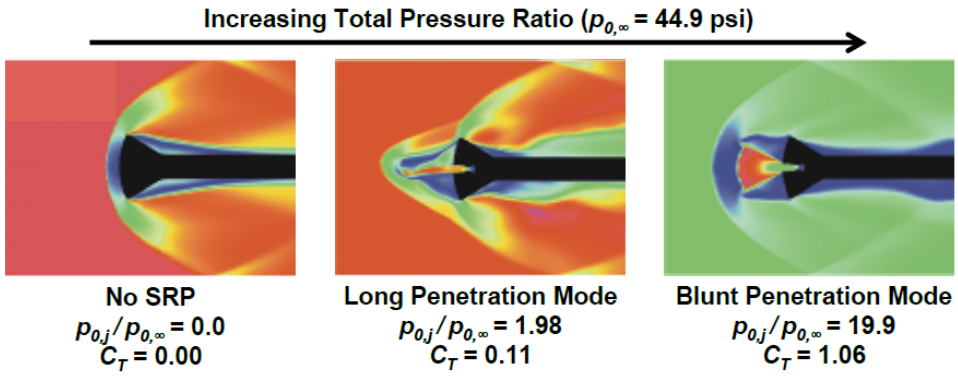

Figure 2.4: Numerical models of SRP flow regimes for increasing stagnation pressure ratios at Ma_∞=3.48 and Ma_{jet}=2.94. [7]

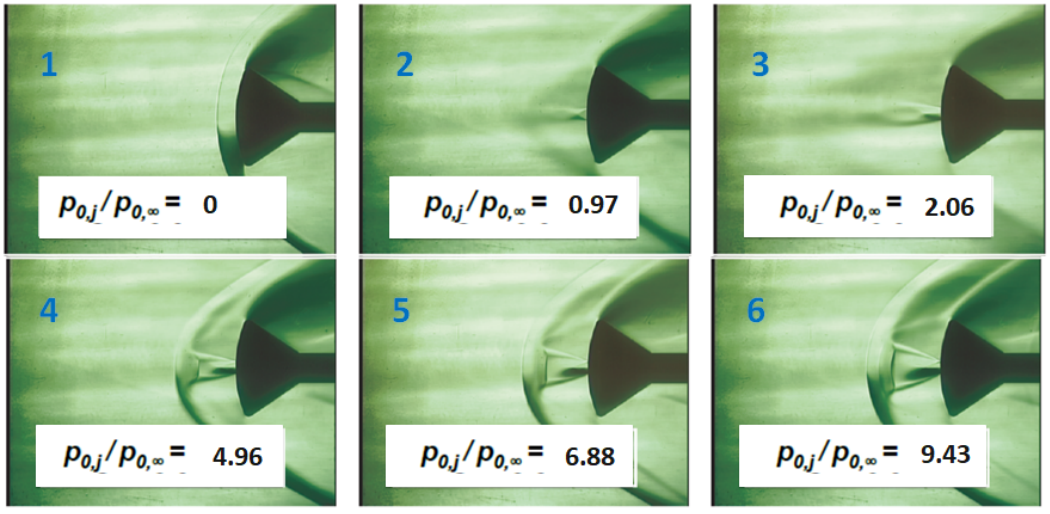

Figure 2.5: Schlieren images of SRP flow regimes for increasing stagnation pressure ratios (from images 1 to 6) at Ma_∞=3.48 and Ma_{jet}=2.94. Adapted from Daso [7].

Korzun [10] also found that the value of C_A in computational models of SRP flow oscillated at frequencies around 1800 Hz depending on flow conditions and retronozzle configuration. A common parameter incorporating oscillation frequencies is the Strouhal number. The Strouhal number is a non-dimensional number which can be useful for comparing unsteadiness between different studies. Korzun calculated Strouhal numbers for the computational frequencies found in her study, all of which were all $\mathcal{O}(10^{-1})$. For the purposes of this study, the Strouhal number is defined as follows to match Korzun's definition:

$$St = \frac{fD}{U}$$

Here, f is the frequency of shock oscillation, D is the retronozzle diameter, and U is the freestream velocity. Other choices of characteristic velocity or lengthscale may prove more applicable to SRP flow but at present there is insufficient data to make a determination.

2.2 Previous Experiments at the University of Washington

This study is a continuation of the work done by Tan in 2018. Stagnation pressure ratio was retained as one of the primary parameters investigated in this study. Tan [8] found that unsteadiness occurred at a $P_{0,jet}/P_{0,\infty}$ value of one for a simple retronozzle setup with a freestream Mach number of 2. It was also shown that the long penetration mode found in previous studies was not required for unsteadiness to be present in the flow field, which further motivates the investigation of forebody scaling for this study. Instead, at a $P_{0,jet}/P_{0,\infty}$ of one, a possibly new type of unsteadiness was observed wherein the bow shock moved as a single coherent structure. Frames from video of this phenomenom can be observed in Figure 2.6.

Tan's study did not address whether this type of unsteadiness was observed due to the relative size of the nozzle to the freestream, nor did it examine what the frequencies of unsteadiness might be. Tan's use of a single nozzle configuration also leaves the question of

whether increasing forebody would immediately result in a more expected penetration-type unsteadiness.

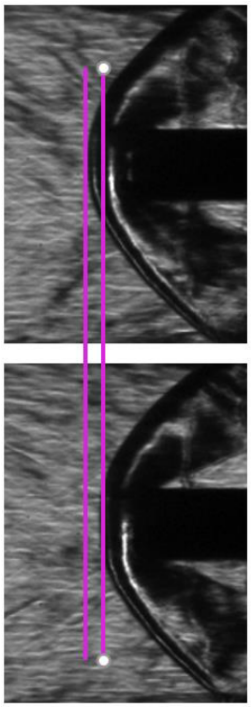

Figure 2.6: Bow shock oscillation for $P_{0,jet}/P_{0,\infty}$=1. [8]

Chapter 3
METHODS AND MATERIALS

The data set used in this study was comprised entirely of high-speed imagery. All images were collected via a camera capturing schlieren imagery of the confluence region created by the interaction of a supersonic jet exhausting into a larger freestream flow.

3.1 Ludwieg Tube

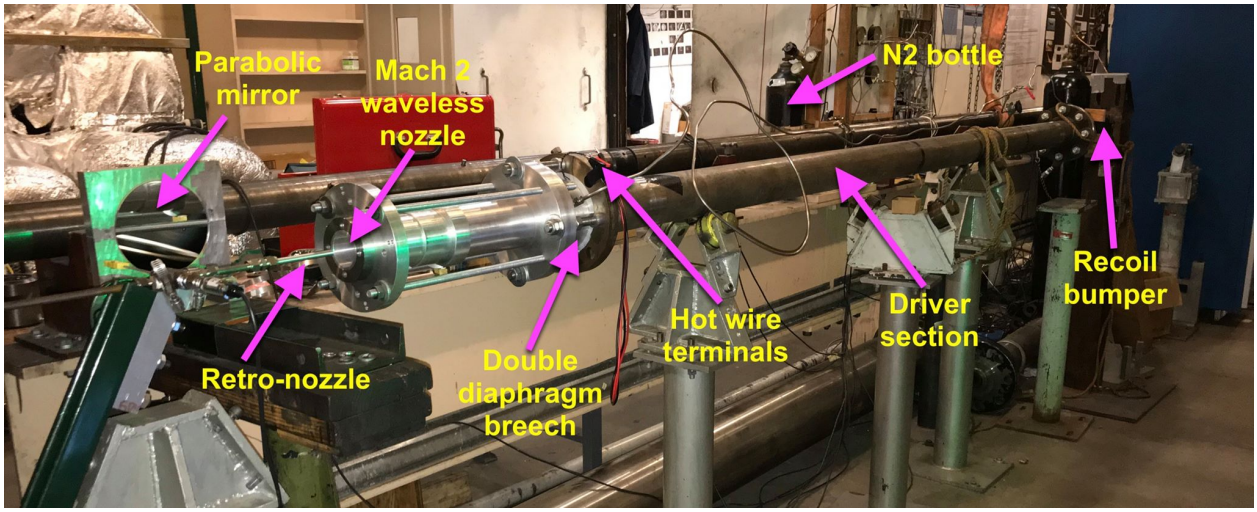

Figure 3.1: Diagram of Ludwieg tube and test section.

The freestream flow was provided by a 10 ft Ludwieg tube. The Ludwieg tube was equipped with a waveless nozzle designed to produce Mach 2 flow from a 2 inch exit diameter and has an effective runtime of approximately 16 milliseconds. Nitrogen gas was used as the working fluid for all of the experiments and was stored in K-type cylinders nearby. The arrangement of the Ludwieg tube, test region, and retropropulsive jet can be seen in Figure

3.1.

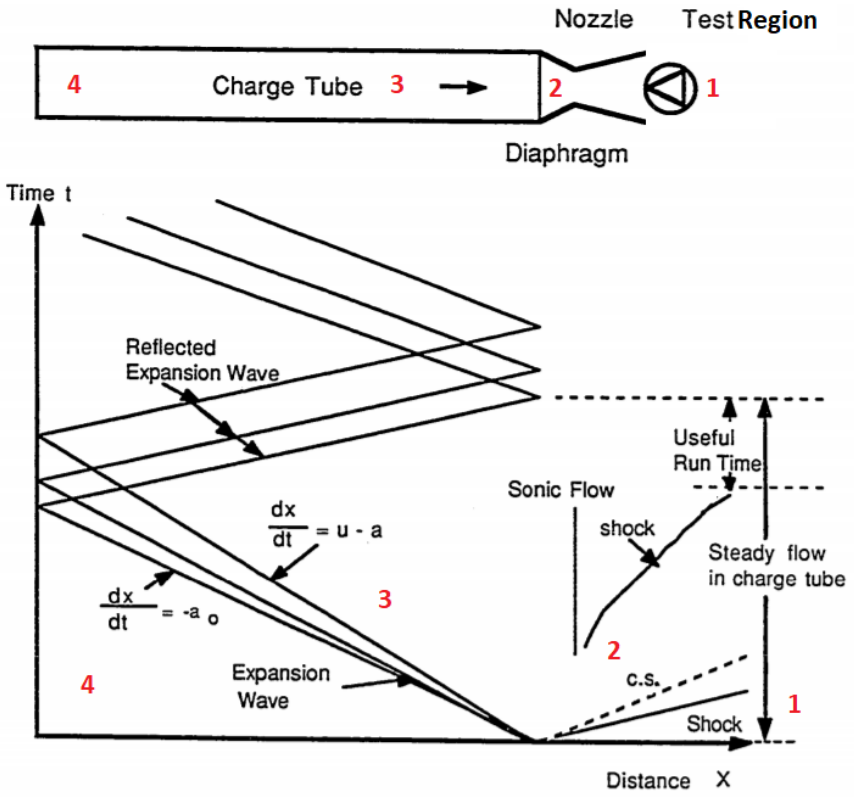

Figure 3.2: x-t diagram for a Ludwieg tube with a closed test section. [15]

The mechanics of a Ludwieg tube are similar to that of a shock tube with the inclusion of a converging-diverging nozzle to further accelerate the freestream flow. The driver section of the tube is filled to the chosen stagnation pressure and is separated from the nozzle section by diaphragm. The diaphragm, in this case made of 7.5 mm thick mylar, is capable of sustaining a pressure differential greater than that between the driver section and the nozzle section. To trigger the start of the flow, a nichrome wire was used to burn an incision into the mylar diaphragm such that it would be weakened to the point of bursting. The x-t diagram of a Ludwieg tube can be seen in Figure 3.2 with regions labeled one through four. The diagram shows the propagation of expansion waves and shocks throughout the system

and illustrates the bounds of useful run-time for a Ludwieg tube wind tunnel. The run time of the Ludwieg tube is set by the time it takes for the expansion waves to be reflected and reach the throat of the nozzle, the flow produced will be steady until this occurs. All testing for this study was conducted in Region 3. The pressure set in Region 4 determined the flow conditions in Region 3, so it was necessary to tune this pressure such that resultant flow out of the nozzle was perfectly expanded for the ambient conditions of the room.

3.2 Schlieren System

High-speed imagery was collected with schlieren photography. Like previous experiments exploring SRP flow structures, schlieren was chosen because it effectively highlights spatial variations in density, which are characteristic of phenomena like shocks and expansion waves. A schematic of the schlieren system can be seen in Figure 3.3. Notably, a single concave mirror is used to make the system as compact as possible. The light source was an LED which produced pulses of light lasting 1 μs. Pulses of this length were chosen in order to properly freeze the flow structure captured in each frame of the high-speed video. The light source was developed by Yang (2019) [16] based on the system designed by Lincoln [17]. Schlieren images were captured using a Vision Research Phantom v1121 high-speed camera. The camera was equipped with a 200mm lens and 2x teleconverter which resulted in an effective focal length of 400mm. The image resolution was 384 pixels by 288 pixels with an exposure time of 1.76 μs and a frame rate of 76,000 frames per second.

Light produced by the high frequency LED was passed through a condenser lens and the converging light was then sent through an aperture which was placed at the focal point with the aim of creating an almost point source of light to be used within the remainder of the setup. The diverging light stream was then sent through a beam splitter all the way to the concave mirror which then reflected the converging light back along the same path to the beam splitter which then reflected the light 90°. A knife edge was placed vertically at the new location of the reflected focal point such that the resulting image captured by the camera highlighted the density gradients in the streamwise direction. The beam splitter permitted

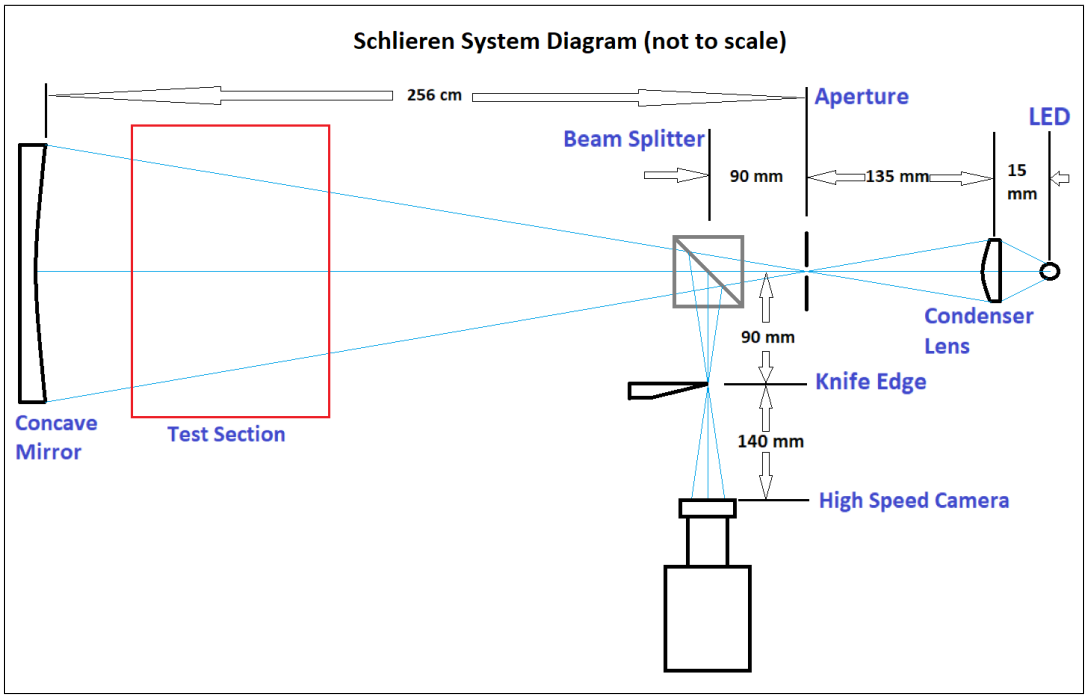

Figure 3.3: Schematic of the schlieren system used for all final data collection.

only half of the light that encountered it through. This resulted in a 75% reduction in image intensity but also allowed for the complete elimination of image doubling since the light was able to follow the same path into and out of the test region. This loss in light intensity could be overcome by increasing the output of the LED. For more information on the schlieren system, see Yang's 2019 master's thesis [16].

The switch that sent current through the nichrome wire to trigger the Ludwieg tube also simultaneously sent a signal to the Phantom camera which caused it to capture the available frames immediately following the trigger signal. This method eliminated any possibility of early or delayed camera triggering, which result in failure to capture the short duration of SRP flow.

3.3 Nozzles & Forebodies

Three supersonic retronozzles, with effectively zero forebody, and two forebodies were manufactured for the purpose of investigating nozzle and forebody size effects on flow unsteadiness. The specifications of each of the retroflow apparatuses can be seen in Figure 3.4. The three retronozzles were 3/8", 1/4", and 1/8" in outer diameter. The nozzles themselves were made using a constant angle custom cutting bit and are thus conical with an expansion angle of 4°. The amount of forebody for each retronozzle was minimized. This resulted in retronozzle jet diameter to forebody diameter ratios of 0.656 for all of the retronozzles. The nozzle exits were centered for each body. Each of the nozzles were designed with throat-to-exit area ratios that would produce a Mach 2 retrojet. The three bare retronozzles will be collectively referred to as "simple nozzles" throughout this document.

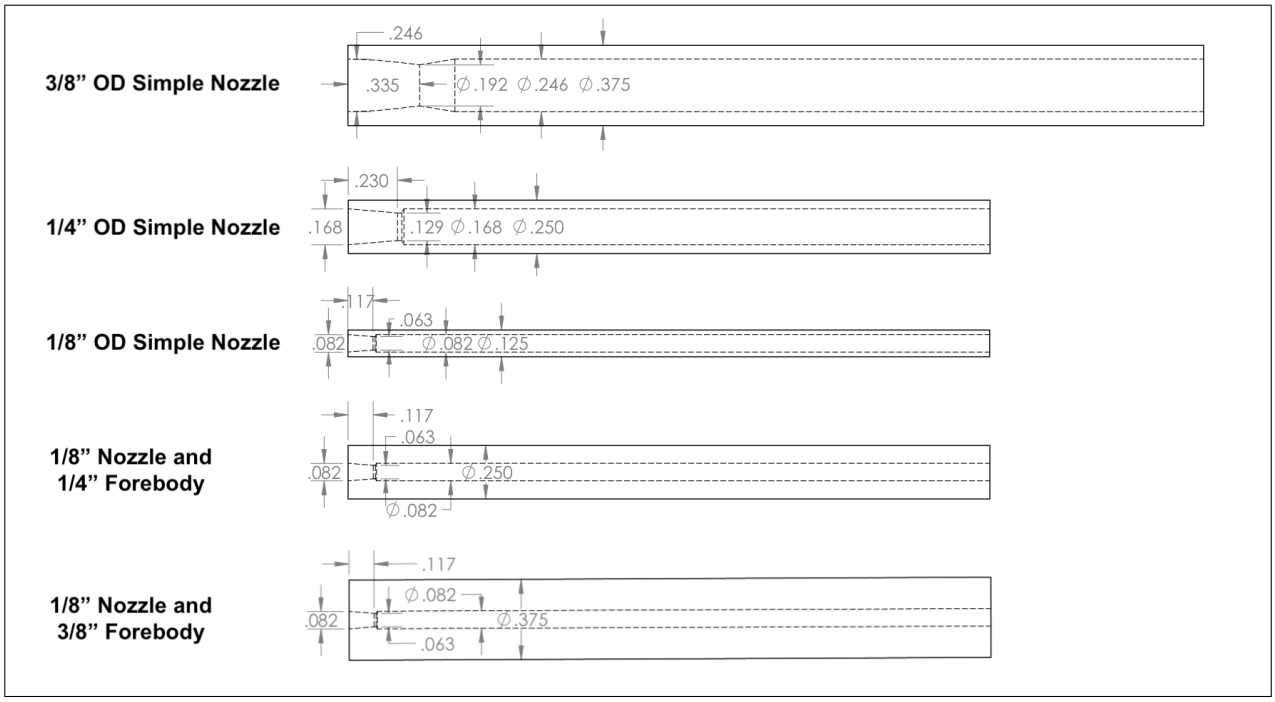

Figure 3.4: Cutaway drawings, to scale, of each of the nozzle and forebody combinations used.

The additional forebodies were made such that they would fit as sleeves around the 1/8" retronozzle. The new outer diamater would either be 1/4" or 3/8" depending on which forebody was attached. Regardless of the forebody configuration, the retronozzle-forebody assembly would still produce the same retrojet as the bare 1/8" retronozzle. The 1/4" forebody and 3/8" forebody configurations had jet-to-forebody area ratios of 0.108 and 0.049, respectively.

Chapter 4

IMAGE ANALYSIS

A series of high-speed schlieren videos were aquired for each retrojet configuration. The Phantom high-speed camera output the data as a series of frames stored in a *.cine* format. The frame rate of the camera, the effective run-time of the Ludwieg tube, and the conditions of the flow resulted in a usable number of consecutive frames ranging from approximately 200 to 1000. For each case investigated, the videos needed to be processed in order to yield quality mean and rms images as well as to aid in the extraction of shock oscillation frequencies in the unsteady cases. This involved mitigation of the motion of the retronozzles under the impulsive freestream loading caused by the startup of the Ludweig tube so that the nozzle stayed in a fixed location within each video. The motion of the bow shock would then be extracted and its frequencies asessed. All image manipulation and processing was conducted in MATLAB.

4.1 Motion Tracking & Pre-processing

First, data was imported into MATLAB by using suite of functions provided by Vision Research, the manufacturers of the high-speed camera. These functions allowed for the extraction of individual frames and video properties and the storage of that information as manipulatable matrices.

All cases exhibited some retronozzle motion which complicated the assessment of shock motion relative to the nozzle. The motion was produced by the impulsive loading of the Ludweig tube startup. Efforts were made to limit nozzle motion through adjustment of the rigidity of the experimental setup. These included tightening the retronozzle stand to the floor and modifying the how the retronozzle was secured to the stand. However, some

motion persisted. The effects of the retronozzle dynamics were particularly apparent in the 1/8" retronozzle cases, to the point where the nozzle tip would move several nozzle diameters vertically and horizontally over the course of the video. Failure to account for this motion would pollute the calculation of mean and RMS images and significantly hamper frequency extraction. Thus, it was necessary to develop a motion tracking method such that a stabilized video could be created. The method needed to accurately track the nozzle through the majority of the frames and model the tip position smoothly. The nozzle motion was assumed to be smooth and, as a result, extracted nozzle positions were also smoothed so that high-frequency motions were not erroneously introduced into the stabilized videos.

Isolating the nozzle such that it could be accurately tracked proved to be a challenge. Many methods of filtering and classifying were examined but only one proved robust enough to satisfactorily separate the nozzle from the rest of the image for all frames and all cases. The 1/8" retronozzle cases in particular were the most difficult to process as they had the lowest resolution and smallest amplitude of bow shock oscillation. The equal pressure 1/8" retronozzle case was chosen as the representative case, it is assumed that a tracking method that works for this case will work for all cases in this study.

It was eventually found that machine learning methods exhibited the greatest ability to separate the nozzle from the flow across all nozzle sizes. Specifically, k-means image segmentation showed the greatest promise. The function *imsegkmeans* was used with 2 clusters. Figure 4.1 below demonstrates the ability of k-means segmentation to separate the nozzle from the rest of the image for the representative case discussed above. The method was able to pick out the nozzle and therefore was implemented as part of pre-processing for motion tracking.

Once the nozzle was isolated for all frames it was then necessary to create a method to track the nozzle itself through time and two spatial dimensions. This was accomplished by choosing a single row and a single column of pixels for each case that would be investigated across all frames. The row and column of data would be checked for a number of consecutive white pixels commensurate with the size of noise observed in the frame to confirm the

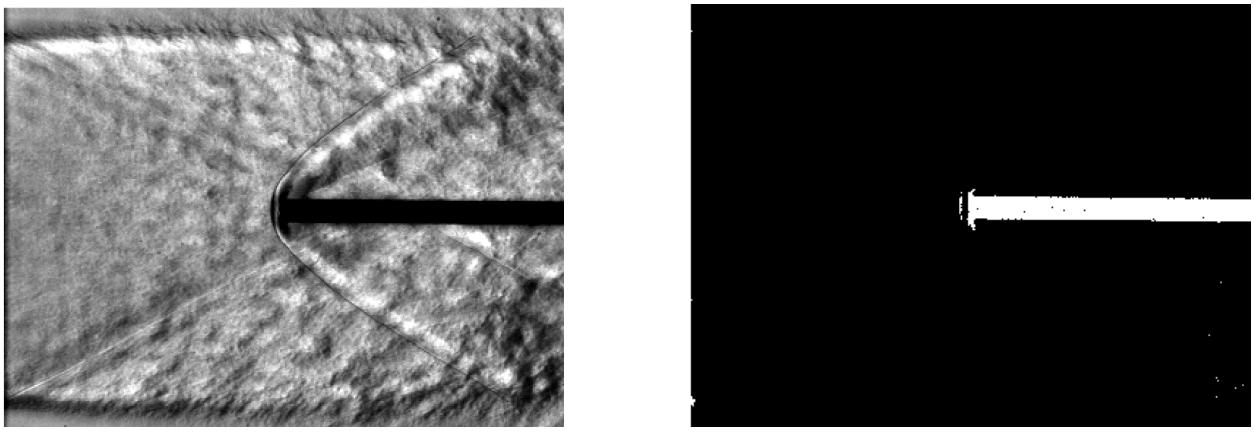

(a) (b)

Figure 4.1: (a) An unprocessed frame imported from raw .cine file. (b) A binarized form of the same frame obtained using K-means segmentation.

presence of the nozzle. Any noise encountered was passed over as it would not meet the consecutive pixel criteria. The location of the column and row to be interrogated was chosen by overlaying the first and last frame for each case. An example of this overlay can be seen below in Figure 4.2, here a point which would determine the column and row to be investigated would be chosen to fall within the white region.

For the column of interrogation data, the average location of the white pixels is taken to be the y-location of the nozzle tip. For the row of interrogation data, the first white pixel that hasn't been passed over would be taken as the x-location of the nozzle tip. This process was repeated for each frame and the x- and y-locations were stored. The modeled x- and y-position data were smoothed by applying polynomial fits to the sensed location data. A linear fit was applied to the x-direction and typically a third or fourth order fit was applied to the y-direction. The order of fit was determined by inspection of the raw sensed data and was dependent on the nozzle type due to variations in geometry, mounting, and video duration. The modeled and extracted nozzle tip locations can be seen in Figure 4.3.

Figure 4.2: The first and last frames of the representative schlieren recording overlain.

Each frame was stabilized and cropped so that the nozzle tip would lie at the center of the video. This was accomplished by determining the closest vertical and horizontal approach of the nozzle tip over the course of the video to the original boundary of the frame using the modeled tip location and removing the pixels that fall between the closest approach and he original edge of the frame in both directions. Cropped frame examples from the representative case can be seen in Figure 4.4.

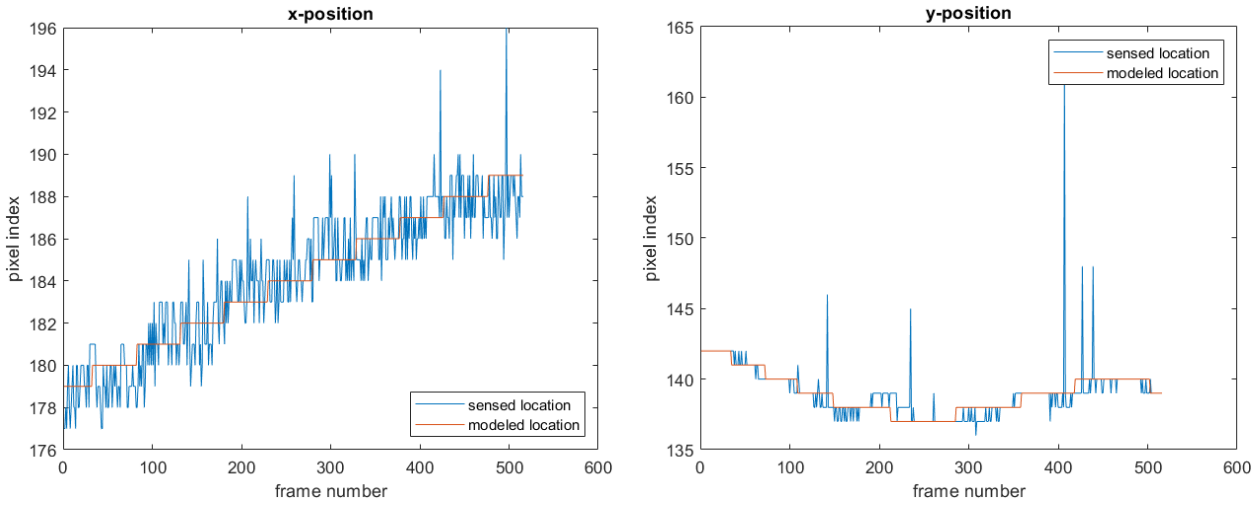

(a) (b)

Figure 4.3: (a) Tracked and smoothed horizontal position of the nozzle tip. (b) Tracked and smoothed vertical position of the nozzle tip.

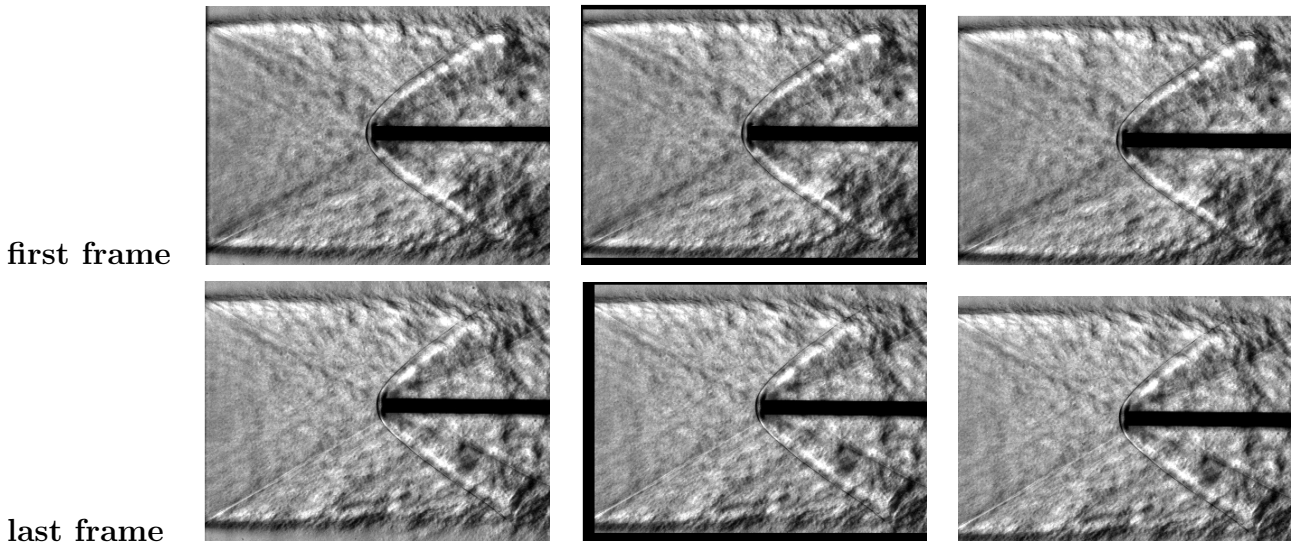

Figure 4.4: The left images show the original uncropped frames, the middle image show the same uncropped frames from the left images with the regions to be cropped shown in black, and the right images show the cropped frames.

4.2 Frequency Extraction

The stabilized, centered videos facilitated the creation of an effective frequency extraction method. The goal was to filter each stabilized and cropped video in such a way that the bow shock would be distinct and the background noise would be mitigated. This would allow for the detection of the shock location in each frame and plotting of its movement through time which would in turn allow for frequency analysis. The MATLAB function *edge*, using the *Roberts* method setting, was applied to each frame of the video for each case. This was done to highlight the portions of the frame which exhibited the greatest pixel intensity gradients. Because shocks are by nature discontinuous, edge detection methods pick them out well while turbulent noise may be removed by careful selection of the gradient threshold. The Roberts approximation to the derivative was used. A representative *edge* filtered frame can be seen in part (a) of Figure 4.5 below.

Once filtered, the shock location needed to be determined. Ideally, this would be accomplished by examining a single row of pixels and selecting the first encountered white pixel as the shock location. However, the edge-detection method still admits some turbulent noise in front of the shock which register as false positives. Additionally, for many cases, the first dozen or so lefthand pixels can show parts of the Ludwieg tube nozzle edge. To curb the effects of these phenomena on resulting frequency content estimates, the investigated pixels were restricted to those shown in part (b) of Figure 4.5. For each unity stagnation pressure case, the rows of pixels ranging from the top of the projected retrojet area to the bottom of the retrojet were used to determine the shock location.

Each row was treated as an independent signal. The shock location was taken to be the first white pixel reported in each row. An outlier detection function, *isoutlier* with the *movmedian* setting selected, was applied to that row of data to throw out false positives. In addition, while the motion tracking and cropping were effective in eliminating the greatest proportion of signal noise, a small quantity of low-frequency drift remained. This necessitated the application of a moving mean to each of the signals which helped get remove low

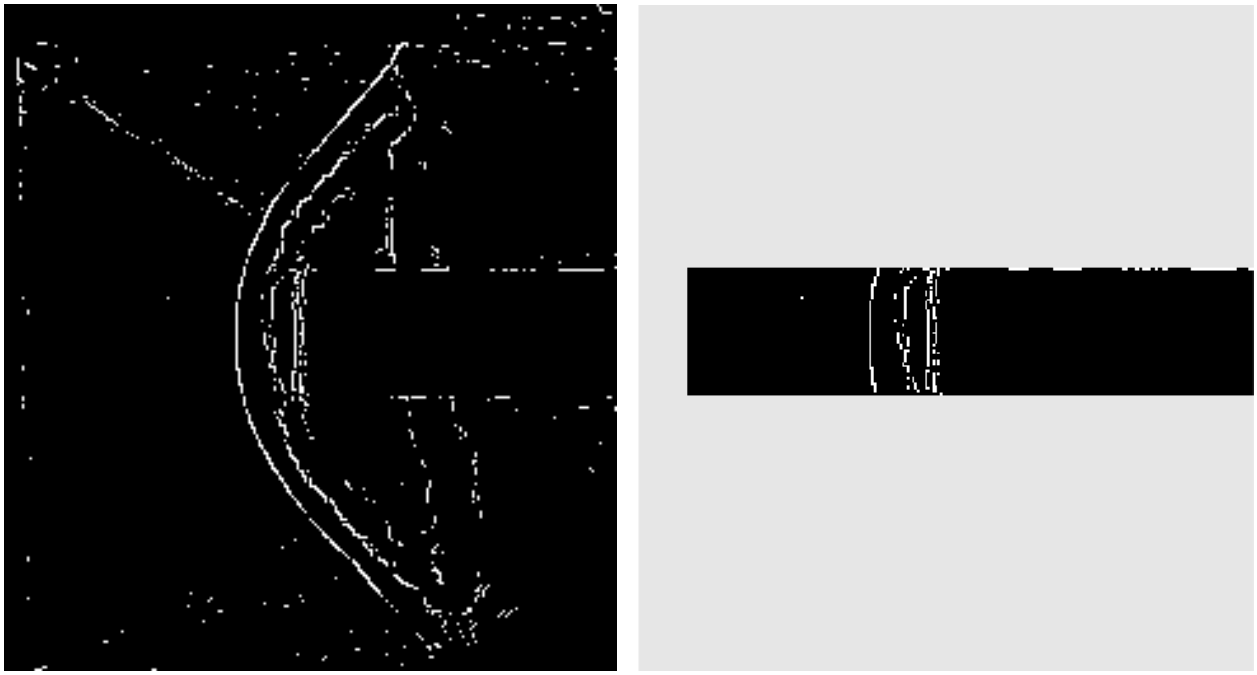

(a) (b)

Figure 4.5: (a) Frame from the 3/8" retronozzle equal pressure case after being put through an edge detection filter. (b) The rows of pixels from that frame which were used for shock detection.

frequencies of $\mathcal{O}(1)$ Hz. The moving mean was implemented using the function *movmean* with the specification that each row of data should have the mean position across a window of 25 frames subtracted from the data set.

A median signal was then distilled from the individual row signals by taking the median value of the shock location reported in each row for each frame. This step was designed to further mitigate the effects of outliers on the final shock position signal. The individual and median signals for the equal pressure 3/8" retronozzle case can be seen in Figure 4.6. The figure illustrates the effectiveness of the median method in eliminating outlier points from the individual signals. It should be noted that this method only works for cases where it

can be assumed that the shock motion is coherent for the region under examination. Also note that each of the signals is centered at zero due to the application of the moving mean subtraction.

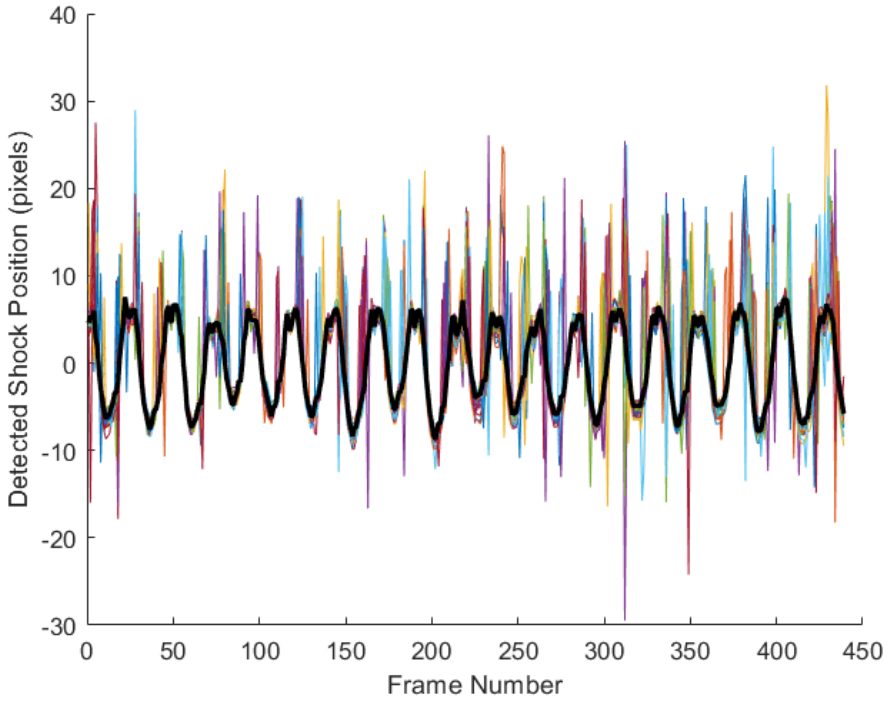

Figure 4.6: Detected shock location for all signals for the 3/8" retronozzle equal stagnation pressure case with the median signal in bold black.

Once the shock location was plotted across all frames, the next step was to use that data to determine a frequency spectrum for the bow shock motion. This was done using the MATLAB function *pwelch* which is a spectral estimator. Figure 4.7 shows the frequency spectra for the same case as shown in Figure 4.6. The figure demonstrates that while, for this case, many of the individual signals exhibit their most prominent peak at the median value of 3265 Hz, the median signal maintains the prominence of the individual frequency peaks while also washing out the other prominent frequencies which had appeared in the

individual signals.

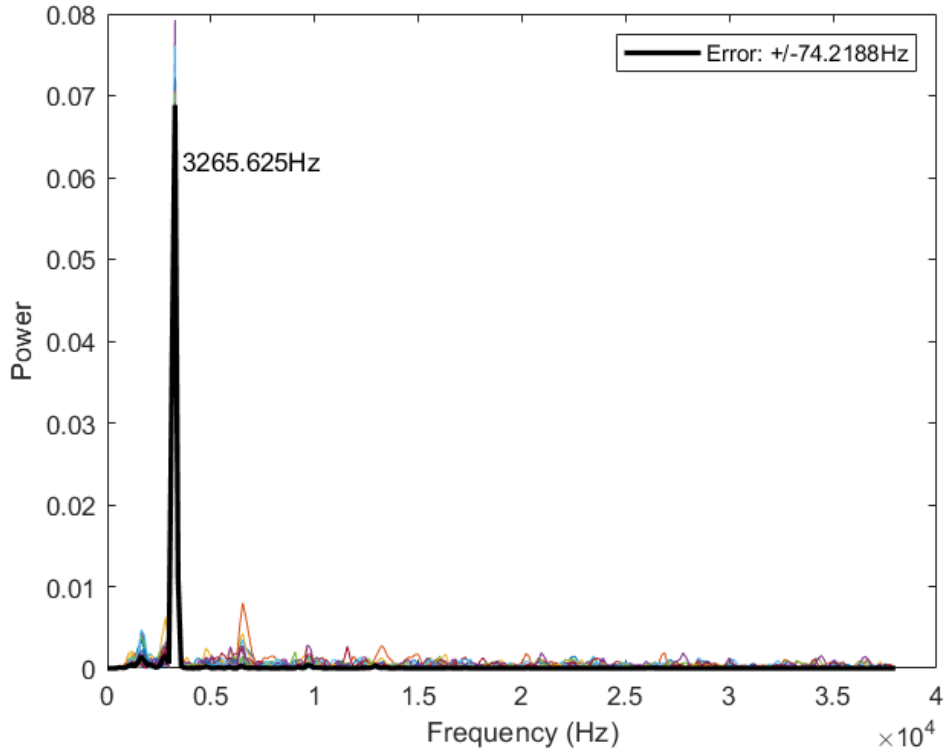

Figure 4.7: The frequency spectra for each of the signals from the 3/8" retronozzle equal pressure case with the median signal spectrum in bold black.

Strouhal numbers were calculated for all unsteady cases. The diameter of the embedded jet was selected as the characteristic length in all cases. The velocity was calculated for the Mach 2 freestream using the Ludwieg tube equations and by assuming that the stagnation temperature of the fluid in the driver section of the Ludwieg tube is the same as the ambient temperature just before the test run of that case.

4.3 Challenging Cases

Challenges were encountered when generalizing the frequency extraction process to all unsteady SRP cases due to reductions in resolution and unsteadiness magnitude. As the physi-

cal size of the retrnozzles were reduced, i.e. taken from 3/8" down to 1/8", the size of nozzles in pixels resolution were also reduced significantly. As can be seen in Table 4.1, the pixel height of each nozzle reduced by 16 pixels with each step. This had significant effects on the resolution of the data, considering the 1/8" is itself only 16 pixels wide. Additionally, as the the size of the retronozzles decreased, so too did the oscillation amplitude. For the 1/8" case the shock would only move approximately 3 or 4 pixels.

Raw Signal Percent Miss			
Equal Pressure Case	Rows	Outlier % Per Row	Frames Available
3/8" Retronozzle	48	3.0–8.0%	439
1/4" Retronozzle	32	10.0–16.3%	811
1/8" Retronozzle	16	18.0–25.6%	516

Table 4.1: The highest and lowest percent of frames for which a placeholder (NaN) was assigned for all rows of data in each case, as well as the number of rows of data for each case and the total number for frames for each case.

The individual signals used to calculate the median value of the shock position included placeholders, specifically NaNs, for values which were determined to be erroneous via the methods described earlier in this chapter. Table 4.1 shows how the number of placeholders assigned across the constituent signals in each case rose significantly as the nozzle size decreased, adding about 8% more data loss with each each 1/8" reduction in diameter. The negative effects of the reduction in resolution can also be seen in part (a) of Figure 4.8. There is much less consensus on the shock location across signals and significantly greater number of erroneous data points when compared to the earlier signals seen in Figure 4.6. However, part (b) of Figure 4.8 demonstrates that the median signal method of shock detection is still capable of picking out the oscillation frequency with 20% more prominence than the next highest peak in the median spectrum. While individual signal spectra may exhibit significant prominence, there is not agreement across the data streams. The median signal is

more representative of the actual shock motion frequency because it accounts for erroneous frequencies which may show prominence in one row of data but not the others. Additionally, the bow shock frequencies for the unsteady simple nozzle cases were estimated by eye and the detected frequencies were each within 15% of those values. For these reasons, the peak median signal frequency was assumed to reflect the actual motion of the bow shock, despite resolution challenges.

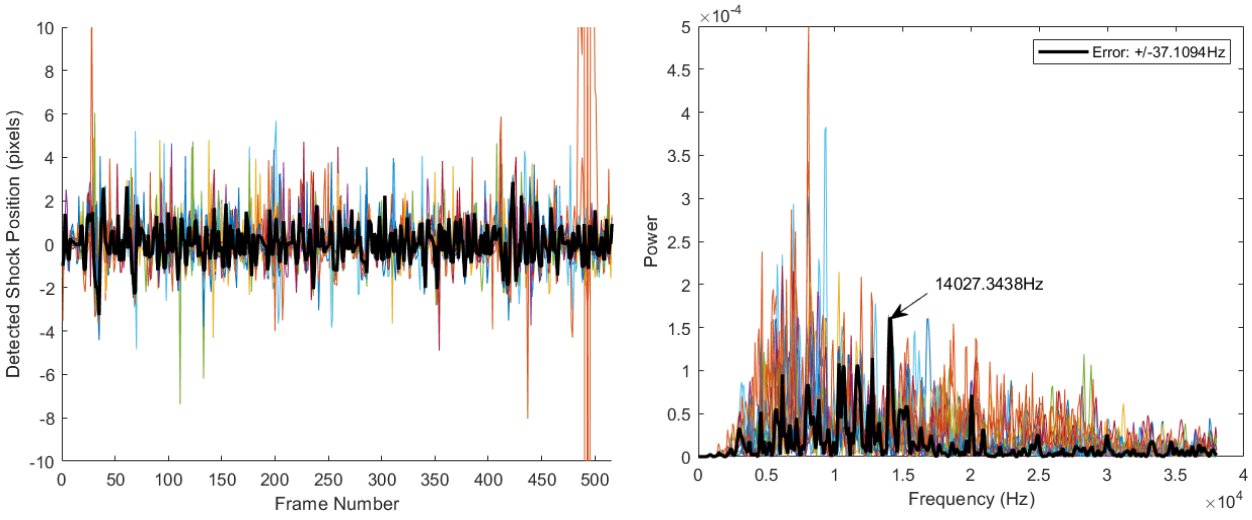

(a) (b)

Figure 4.8: (a) Detected shock location for all signals for the 1/8" retronozzle equal pressure case with the median signal in bold black. (b) The frequency spectra for each of the signals from the 1/8" retronozzle equal pressure case with the median signal spectrum in bold black.

Chapter 5

RESULTS

To investigate the effects of retronozzle scaling and forebody size on SRP flow fields, all retronozzle configurations were tested at $P_{0,jet}/P_{0,\infty}$ ratios of 0.5, 1, and 5. A total of 15 test cases were acquired.

Mean and root-mean-square deviation (RMS) images were produced to help define regions of unsteadiness as well as to highlight the flow structure. The number of frames used for these images was truncated to the first 200 to limit the influence of any changes in nozzle angle of attack due to nozzle motion and to ensure all cases had an equal sample size. The change in angle of attack was small (less than 5° for the most severe case) but the effect on the mean and RMS images was noticeable for the longest datasets. The tracking method used to stabilize the videos resulted in a significant improvement in the quality of the mean and RMS images over Tan's (2018) previous results [8]. The difference in clarity can be seen in Figure 5.1.

5.1 Simple Nozzle Cases

This section will examine significant flow features and trends across the range of stagnation pressure ratios, as well as assess the influence of relative jet and freestream sizes on resulting flow structures. The variation in mean and RMS field with stagnation pressure ratio for the simple nozzles are shown in Figures 5.2 & 5.3 below.

Figure 5.4 points out significant features of the RMS flowfields, common to most pressure ratios and geometries. Shock standoff distance increases significantly with increasing stagnation pressure ratio for all simple nozzle scales. There are also regions of expansion emanating from the edges of the retronozzles, corresponding to a brighter image and higher RMS in

this region. At $P_{0,jet}/P_{0,\infty}$=5 a triple band of high RMS variation can be observed in the bow shock region, which is representative of the edges of the shock structure. This feature is present for all three scales of simple nozzle for this stagnation pressure ratio, however it is most evident in the 1/4" and 3/8" cases. The cases for $P_{0,jet}/P_{0,\infty}$=5 also exhibit similarly shaped jet structures and confluence regions directly behind the triple-band region. Similarly, for the cases where $P_{0,jet}/P_{0,\infty}$=0.5, the jet-post-shock confluence exhibits the same low variation (blue) structure directly in front of the nozzle exit and in the shoulder area of the retronozzles across all nozzle scales.

It should also be noted that for the 3/8" case, the ring-like structure (seen most clearly in the $P_{0,jet}/P_{0,\infty}$=0.5 images) represents the meeting surface of the bow shock and the shear layer at the edge of the freestream. This same structure can be seen in the 1/4" case as well, just further downstream. The ring occurs downstream of the nozzle tip and the important SRP structures needing examination. As a result, the confinement of the largest retronozzle within the freestream flow does not significantly influence the SRP structures of interest and all nozzles up to 3/8" in diameter produce results in which the region upstream of the nozzle tip are not significantly effected by the size of the freestream jet.

There is visible similarity in flow structures across simple nozzle scales for each stagnation pressure ratio, with only structural length scales changing. Thus, it is concluded that nozzle size has little significant effect on SRP flow structure.

For the $P_{0,jet}/P_{0,\infty}$=0.5 and $P_{0,jet}/P_{0,\infty}$=5 cases, the red RMS bands for the bow shocks are quite thin and the mean images are overall very sharp. This means that there is little change in the flow structure across frames, and therefore time, of each video for these cases. The steadiness of the flow is also evident by visual inspection in the videos. For these reasons, the cases are classified as steady.

For the cases where $P_{0,jet}/P_{0,\infty}$=1, the red RMS bands are much thicker when compared to the images for the other stagnation pressure ratios. This signifies that there is much more unsteadiness exhibited for this condition across simple nozzle sizes. The RMS bands exhibit near uniform thickness for the entire length of the bow shock, indicating that the entire bow

shock moved instead of a localized region. By eye, it is also clear in the videos that the bow shocks oscillate coherently at what appeared to be a single frequency. This is consistent with the results found by Tan for her previous study of a 3/8" simple nozzle, demonstrating that the behavior observed by Tan is robust to changes in nozzle scale for our setup [8].

It is clear from these results that forebodies up to 3/8" in diameter can be tested in this setup with minimal interference from freestream flow confinement in the region of interest upstream of the nozzle tip.

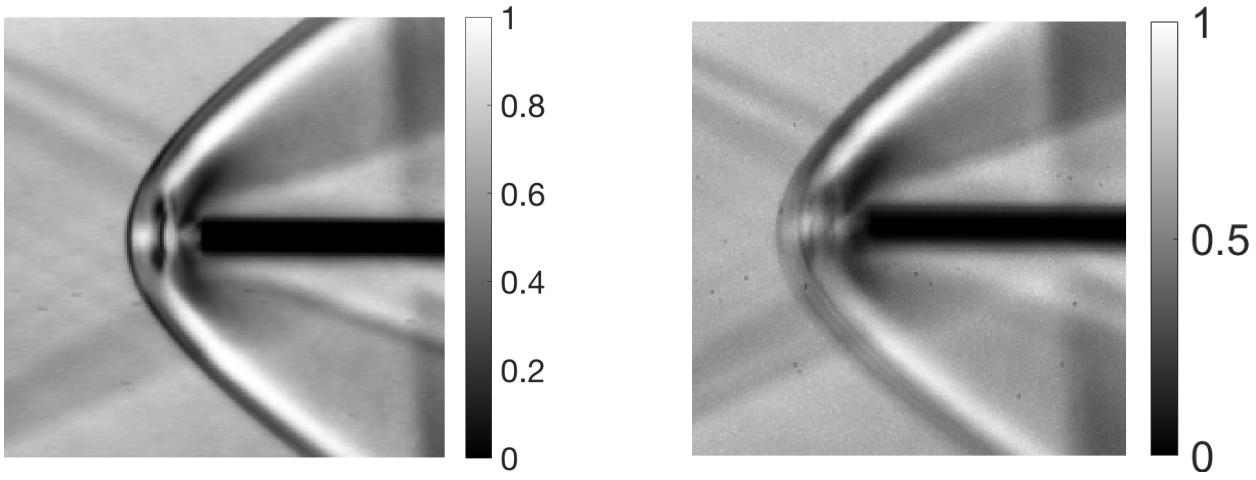

(a) (b)

Figure 5.1: (a) Representative mean image from stabilized video. (b) Mean image from the same case from unstabilized video.

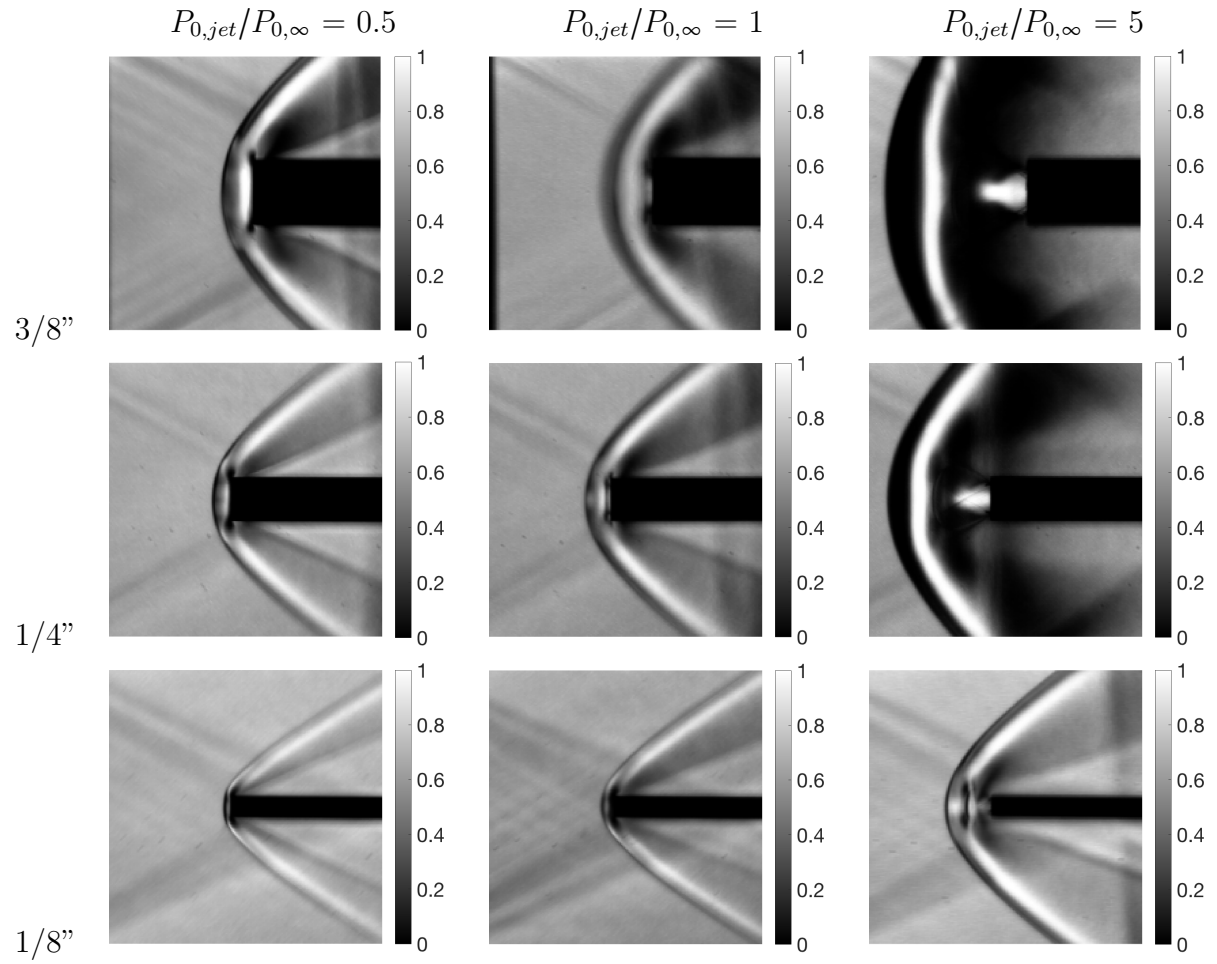

Figure 5.2: The mean images for each of the retronozzles at stagnation pressures ratios of 0.5, 1, and 5.

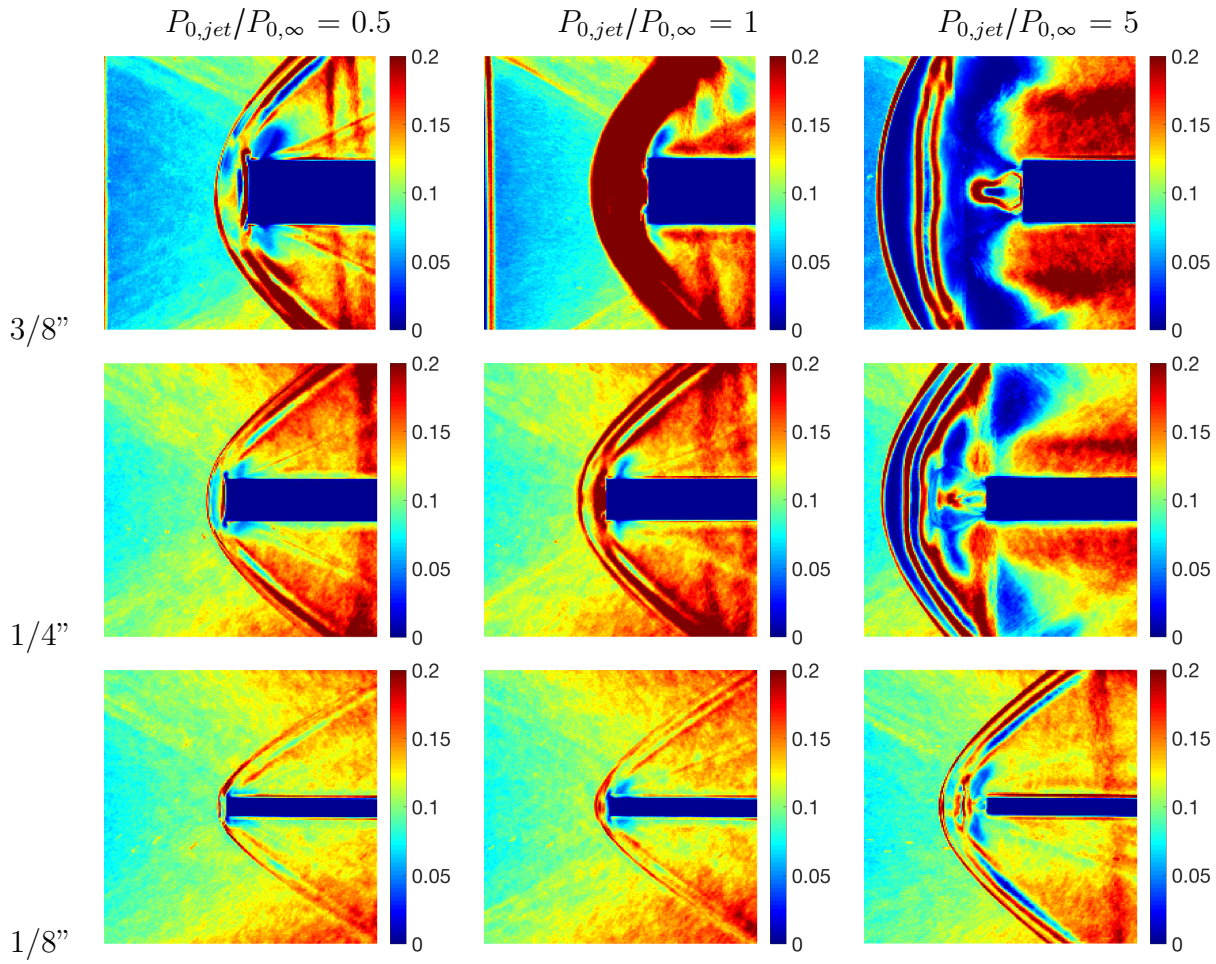

Figure 5.3: The RMS images for each of the retronozzles at stagnation pressures ratios of 0.5, 1, and 5.

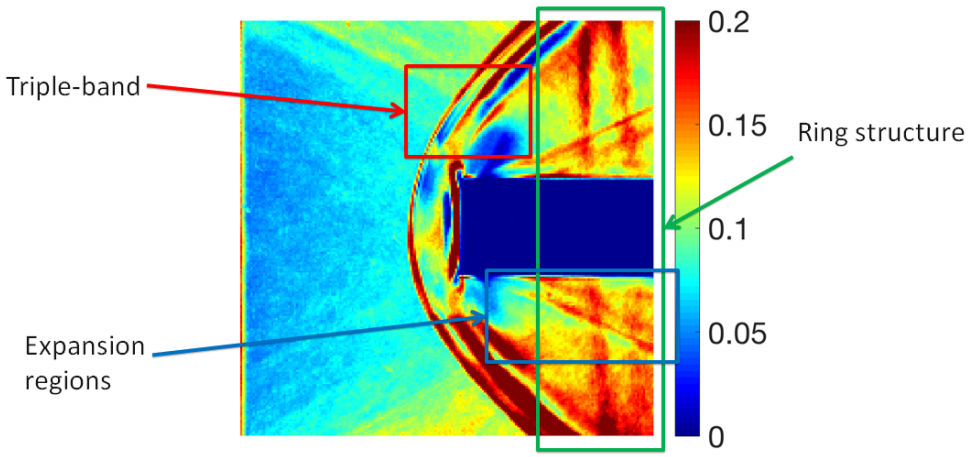

Figure 5.4: Common features of SRP RMS images.

5.2 Forebody Effects

This section examines the effects of jet-to-forebody diameter ratio on SRP flow structure. Figures 5.5 and 5.6 show the mean and RMS images for the 1/8" simple nozzle and the two 1/8" nozzle configurations with additional forebody attachments. Similar to the simple nozzle cases, the flow is steady at $P_{0,jet}/P_{0,\infty}$=0.5 and $P_{0,jet}/P_{0,\infty}$=5 for both larger forebody cases. The bow shocks are smooth in the mean and RMS images for these conditions and no unsteadiness was observed in the videos. Flow features for the steady forebody cases also mimic the simple nozzles, with expansion regions emanating from the forebody edge and the standoff distance of the bow shock increasing with stagnation pressure ratio.

Interestingly, the presence of a forebody results in a different kind of unsteadiness than observed for the simple nozzles. Changes were observed in bow shock curvature for the unity pressure cases. There is a clear bulge visible in front of the retrojet in both the mean and RMS images. There is a localized thickening of the RMS band directly in front of the nozzle for both forebody cases instead of the uniform thickening found for the simple nozzles with no forebody, which suggests dynamic bulging or rippling of the bow shock in that region. Bulges can be observed emerging from the bow shock region in front of the nozzle and then disappearing over time directly in the video, examples of these bulges can be seen in Figure **??**. These results suggest that a different type of unsteadiness, bow shock penetration, is observed where the only difference between these cases and the simple nozzle cases is the jet-to-forebody diameter ratio. These penetrations are not as severe or destructive of the bow shock as those observed in previous studies, but they still fall under the definition of penetration for this thesis.

Figure 5.7 depicts that the mean image for the 1/4" retronozzle case is much sharper in the region directly in front of the retronozzle exit than it is for 1/4" forebody case. Likewise, the RMS image for the 1/4" forebody case shows thicker deep red regions around the bow shock while the 1/4" retronozzle case RMS image has sharper, smoother red regions along the entire bow shock. This indicates that the bow shock in the 1/4" forebody case exhibits more

non-uniformity in its motion than the 1/4" retronozzle case, particularly in the retrojet-shock confluence region. This is an indication that a decrease in (A_j/A_{FB}) for this configuration resulted in a shift from uniform bow shock oscillation to bow shock penetration. The same can be said of the change in flow features observed between the 3/8" simple nozzle and 3/8" forebody configuration, which suggests a relationship between relative forebody size and unsteadiness regime.

Figure 5.8 further highlights the difference in type of unsteadiness. The structure of the shocks captured in these frames are clearly similar to the penetration shown in previous studies. However, previous studies show much more prominent penetration, even complete disruption of the bow shock. It should be noted that the range of bow shock motion appears to be the same for both amounts of additional forebody.

It is unclear if the change in unsteadiness regime is a continuum or an abrupt change with increasing forebody size. However, there is some evidence to support the idea of penetration prominence as a continuum. In previous studies, many of the penetrations completely disrupted the bow shock. Here, bow shock penetration is characterized by a bulging of the bow shock instead of destruction. It is interesting that, for the conditions here, any increase in forebody results in a shift from bow shock oscillation to bow shock penetration and that the penetrations observed here are not nearly as penetrative or destructive of the bow shock. It is likely that these differences are due to the range of forebody sizes investigated for this study.

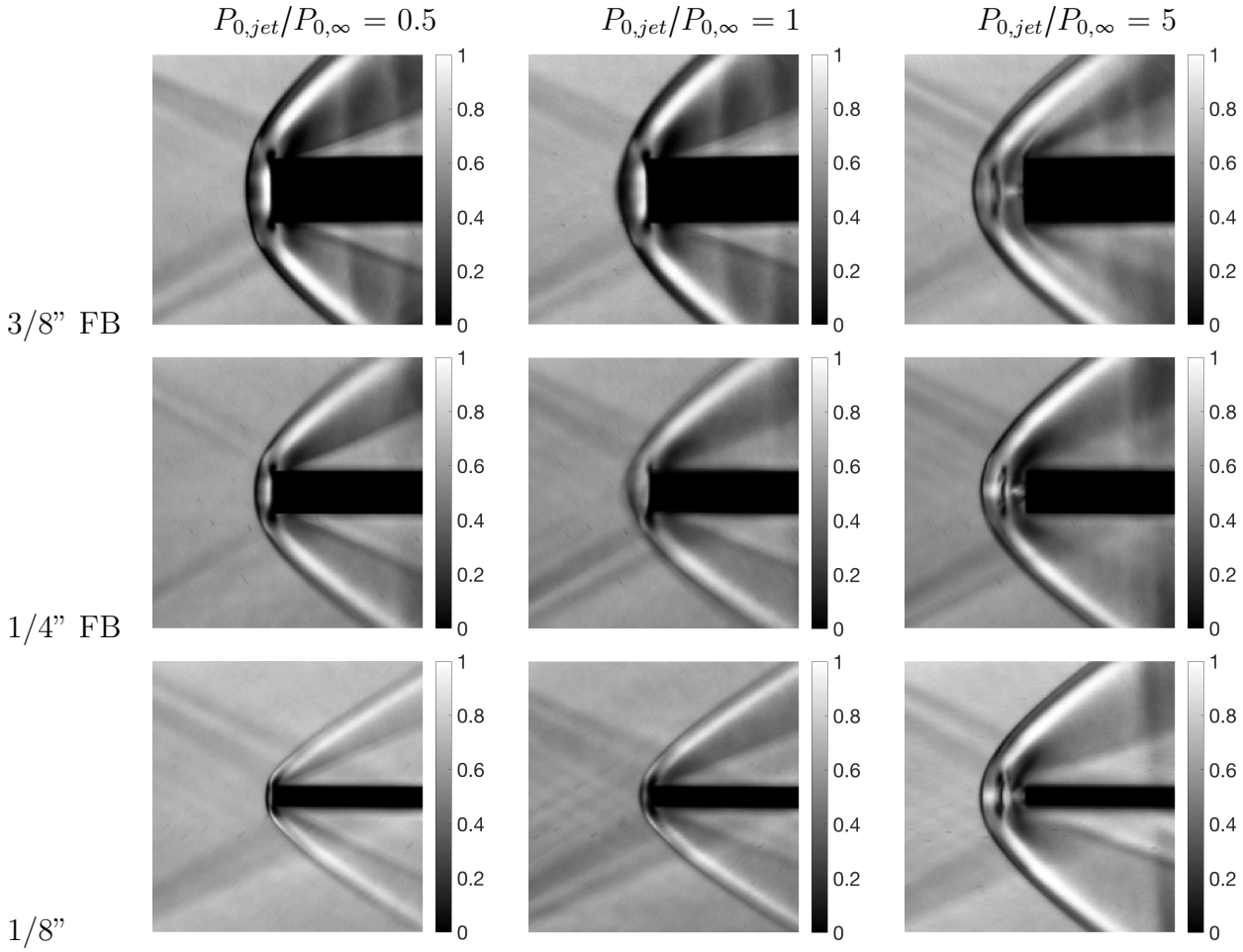

Figure 5.5: The mean images for each of the forebody configurations at stagnation pressures ratios of 0.5, 1, and 5. Note: FB indicates the length listed is the outer diameter of the retronozzle with forebody attachment.

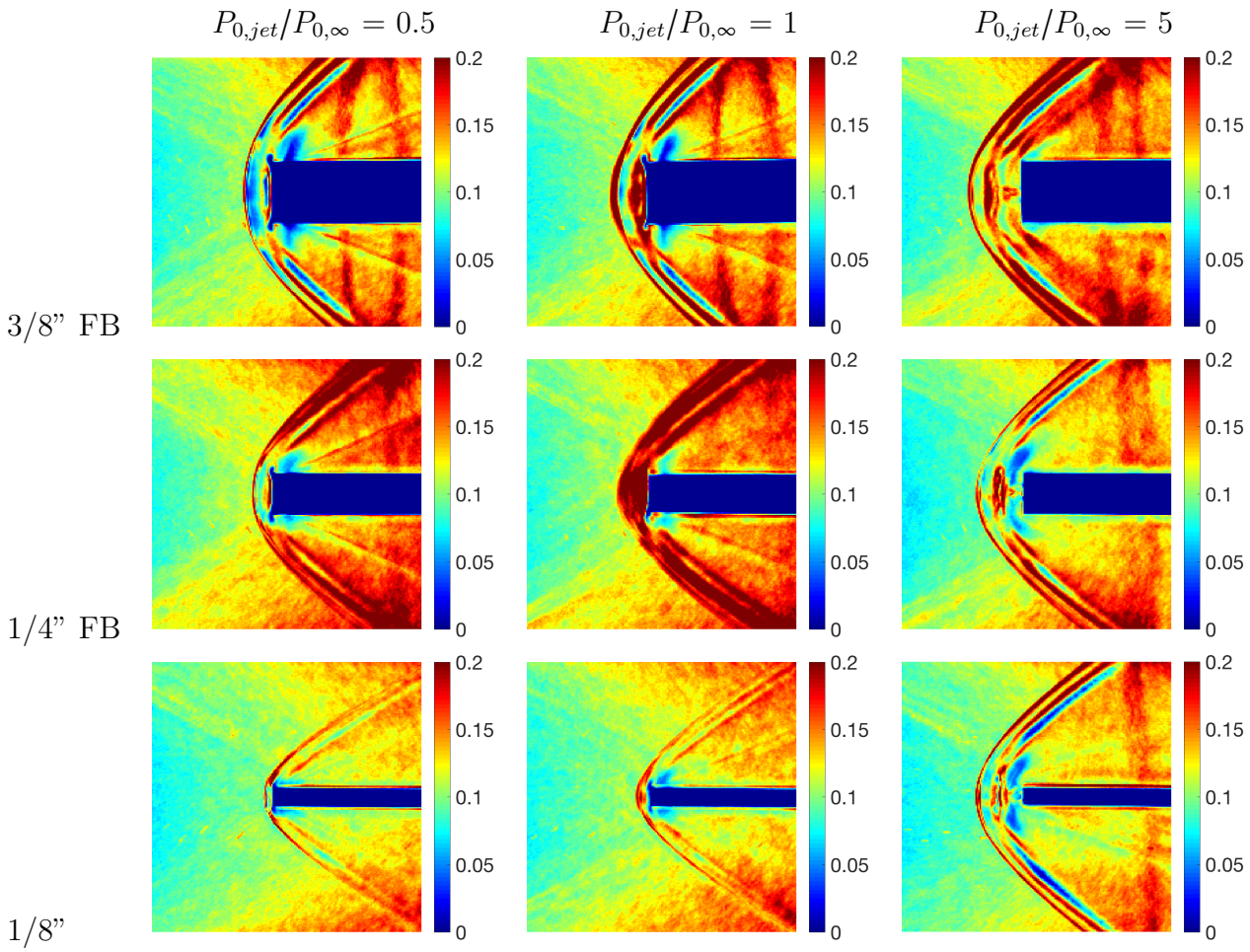

Figure 5.6: The RMS images for each of the forebody configurations at stagnation pressures ratios of 0.5, 1, and 5. Note: FB indicates the length listed is the outer diameter of the retronozzle with forebody attachment.

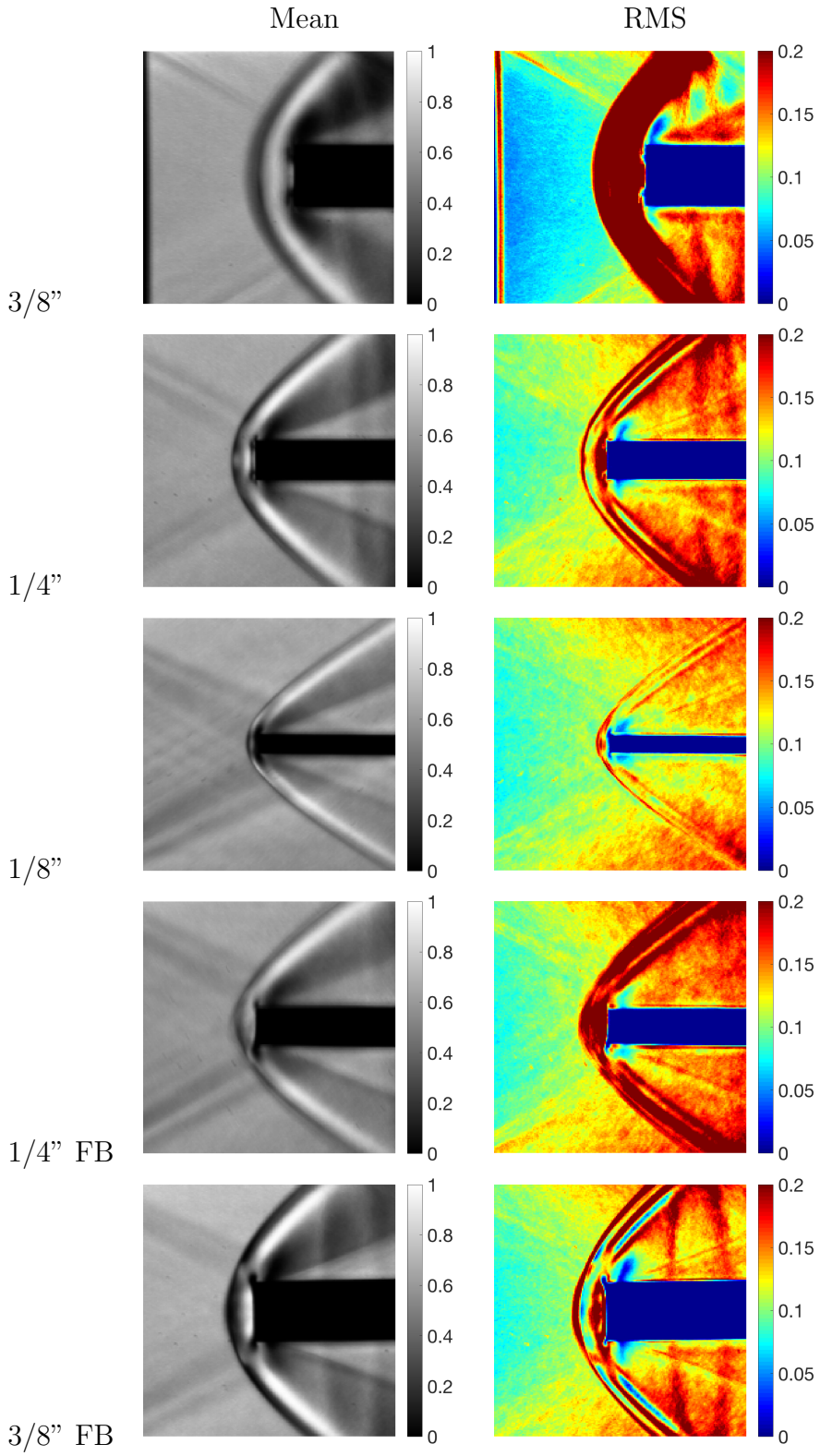

Figure 5.7: The Mean and RMS images for each of the retronozzles and forebody configurations at unity pressure ratio.

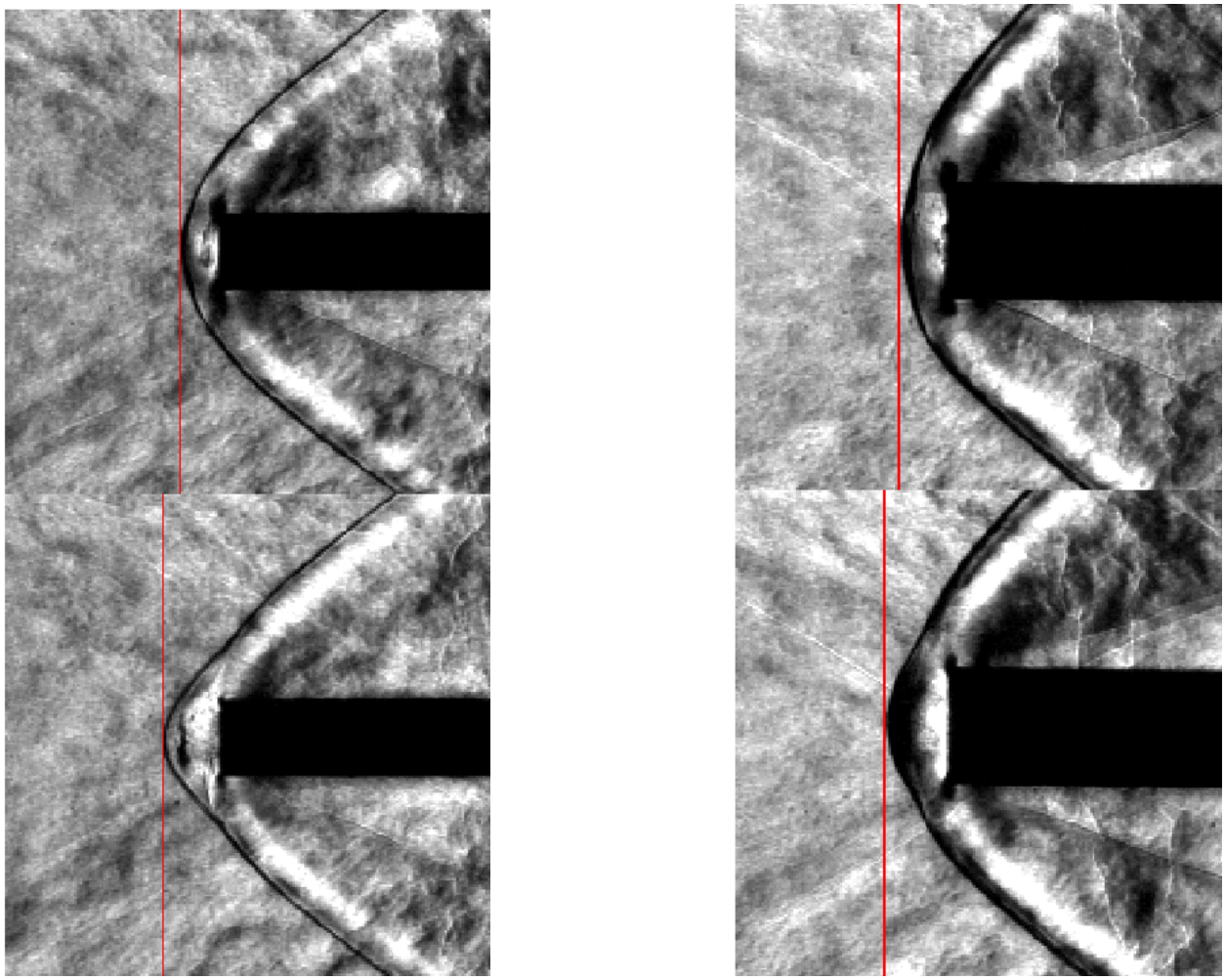

(a) (b)

Figure 5.8: (a) A bow shock penetration from the 1/4" forebody equal pressure case. (b) A bow shock penetration from the 3/8" forebody equal pressure case.

5.3 Unsteadiness

Table 5.1 summarizes the unsteadiness regime classification for each of the tested cases. Unsteadiness was observed in all unity stagnation pressure ratio cases. Two distinct modes of unsteadiness were observed. The simple nozzle cases all exhibited bow shock oscillation while the cases with attached forebodies exhibited bow shock penetration/rippling. The type of unsteadiness appears to be a function of the amount of forebody relative to retrojet size. The 1/8" increases in forebody diameter are associated with the transition from bow shock heaving to retrojet bulging. In fact, penetration appeared as soon as any additional forebody was introduced.

Table 5.2 below shows the dominant extracted frequency for each unsteady case and the associated Strouhal number according to the methods described in Section 4.2. The frequency spectra and plots of the tracked shock motion from which the spectra are derived can be found in Appendix A. For the simple nozzle cases, the frequency extracted is that of the motion of the bow shock. For the cases with forebody attachments, the frequency is that of motion/appearance of the bow shock penetration directly in front of the jet. Once again, these frequencies are derived from the median signals of bow shock motion which rely on coherent bow shock motion in the region of interest. Notably, to the author's knowledge, these are the first frequencies extracted from experimental SRP data.

The frequencies associated with the simple nozzles appear to increase monotonically with nozzle diameter. It is important to note that dominant frequencies were found for all unity stagnation pressure cases. This means that all modes of unsteadiness tested here exhibit periodicity, even those cases with some bow shock penetration. Also of note, the bow shock penetration frequencies are both much closer in value to each other than to the bow shock oscillation frequencies of the simple nozzles. All frequencies detected, however, were within an order of magnitude of each other.

When investigated by eye, the bow shock motion for the unsteady simple nozzle differs significantly from that of the unsteady forebody cases. The simple nozzles exhibited bow

Retronozzle	$P_{0,jet}/P_{0,\infty} = 0.5$	$P_{0,jet}/P_{0,\infty} = 1$	$P_{0,jet}/P_{0,\infty} = 5$
1/8”	steady	unsteady (bow shock oscillation)	steady
1/4”	steady	unsteady (bow shock oscillation)	steady
3/8”	steady	unsteady (bow shock oscillation)	steady
1/8” (1/4” Forebody)	steady	unsteady (penetration)	steady
1/8” (3/8” Forebody)	steady	unsteady (penetration)	steady

Table 5.1: Unsteadiness classification for each retronozzle configuration at stagnation pressure ratios of 0.5, 1, and 5.

shock motion with a single dominant frequency for each case while the forebody cases appear intermittent and more complex at first glance. It is possible that there are multiple significant frequencies associated with bow shock penetration or that the motion frequencies are more broadband than those found here.

Strouhal trends with increasing jet size or forebody size do not exhibit any discernible trends, monotonic or otherwise, at this time. This could be due to a few factors. First, extraction of frequencies for small nozzles taxed the resolution of the images and method. In addition, due to the irregular motion of the forebody cases, sampling error may influence the frequencies extracted and longer datasets would be desired for increased confidence. It is also possible that the chosen characteristic length and velocity scales may not be the best choices. The scales used here were chosen to draw comparison with previous results.

With the results obtained here, it is possible that there exists a single underlying mechanism which drives the oscillatory flow unsteadiness. The Strouhal numbers for all unsteady cases are approximately of $\mathcal{O}(10^{-1})$, which is consistent with the order of Strouhal number reported by Korzun for her computationally derived C_D oscillation frequencies for highly underexpanded SRP nozzles at non-zero angle of attack. Korzun suggests that an annular vortex shedding feedback mechanism is the primary cause of unsteadiness in the flow field for a centrally located nozzle [10]. This inviscid feedback mechanism in SRP flows is also

Retronozzle	Dominant Frequency	St
1/8”	14027 Hz	0.0880
1/4”	8090 Hz	0.1015
3/8”	3265 Hz	0.0614
1/8” (1/4” Forebody)	5789 Hz	0.0363
1/8” (3/8” Forebody)	6457 Hz	0.0405

Table 5.2: Dominant extracted frequencies and Strouhal numbers for each retronozzle configuration at unity stagnation pressure ratio.

observed by Bakhtian et al. [18] in their simulations. In addition, Sobey [19] indicates that for flows with Strouhal numbers between $\mathcal{O}(1)$ and $\mathcal{O}(10^{-4})$ for oscillatory flows between asymmetric channels, the primary mechanism behind oscillation is vortex shedding. So, it may be that vortex shedding is one of, or possibly the only, cause of the periodic unsteadiness observed. However, there is not yet sufficient evidence to draw a firm conclusion.

Chapter 6

CONCLUSIONS

This thesis investigated the effects of retronozzle size and forebody-to-retrojet area ratio on supersonic retropropulsion flowfields. An important aspect of this was the characterization of unsteady SRP regimes and how they are related to forebody size. The results in this study are experimental, derived from high-speed schlieren imagery of the flow interaction region. An analysis method was developed to stabilize nozzle motion due to experimental startup, and extract frequencies and Strouhal numbers from the unsteady flow cases.

It was shown that the 3/8" retronozzle used here, and by Tan (2018) previously, was sufficiently small such that the effects of freestream flow confinement were limitted to regions downstream of the nozzle tip. For the high and low stagnation pressure ratios tested, steady flow was observed for all retronozzle scales. Similar to the results found by Tan (2018), for a matching freestream and retrojet Mach number of 2, each retronozzle size exhibited coherent bow shock oscillation at a jet-to-freestream stagnation pressure ratio of one. Increasing nozzle scale resulted in increased bow shock standoff distance and range of oscillatory motion. Additionally, retronozzle scaling had no apparent effect on the structural organization of the SRP flowfield. Subsequently, all retronozzle or forebodies of this size or smaller could be assumed to not be significantly affected by flow confinement and observed unsteadiness regimes and their characteristics were robust to experimental nozzle size.

Not only was Tan's unsteadiness regime proven to be robust, it meant there was enough space to examine of increasing forebody up to three times the smallest, 1/8", jet size. Under our experimental conditions, increasing forebody area caused a transition from bow shock oscillation to bow shock rippling/penetration. The penetrations observed appeared intermittent and did not completely disrupt the bow shock. This connects the bow shock oscillation

found by Tan and the highly-penetrative type of unsteadiness found in most previous SRP studies. Once again, for the higher and lower stagnation pressure ratios tested, steady flow was observed.

It was found that increasing retronozzle size with no forebody resulted in a decrease in the frequency of bow shock oscillation observed. There is insufficient data to draw any trends from the effect of increasing forebody area on the frequency of unsteadiness at this time. However, the Strouhal numbers for every unsteady case were found to be of $\mathcal{O}(10^{-1})$, which is the same order as Korzun's computational results for SRP force coefficient unsteadiness. Further, these Strouhal numbers fall into the range associated with vortex shedding. So it is possible that both unsteadiness regimes observed here are caused by a common vortex shedding mechanism.

6.1 Further Work Recommendations

The author would recommend some of the following improvements in any continuation of the work done here. First, an increase in image resolution would likely yield more prominent dominant frequencies, particularly for the cases with smaller retronozzles. A related improvement would be an increase in the run time of the experiments. This might help remove some of the nozzle motion dynamics observed here since the nozzle could be allowed to settle into a more stable position before analysis is attempted and also remove questions of spectral sampling bias that result from short runtimes.

Nozzle scaling, forebody size, and stagnation pressure ratio are investigated here but it would also be useful to look at variation of freestream and retrojet Mach number. This would open up opportunities for comparison and validation of previous SRP studies which used different flow conditions than this study. The author also recommends the addition of a particle image veloximetry (PIV) system to the experiment. Application of PIV to SRP flows has never been done before and the results would provide more quantitative data that could be used to help validate and improve CFD modeling of supersonic retropropulsion.

APPENDIX A

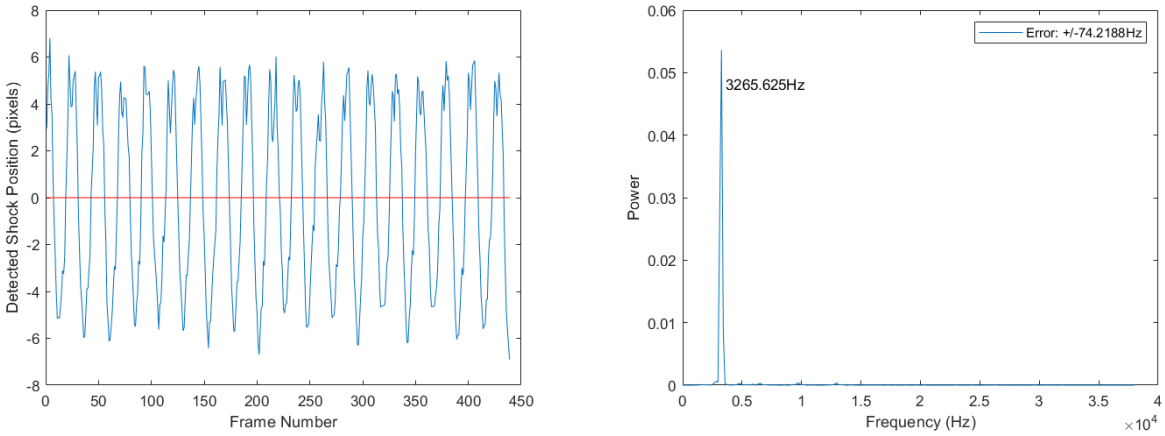

(a) (b)

Figure 6.1: (a) Tracked shock position for the unsteady 3/8" retronozzle case. (b) Frequency spectrum for the unsteady 3/8" retronozzle case.

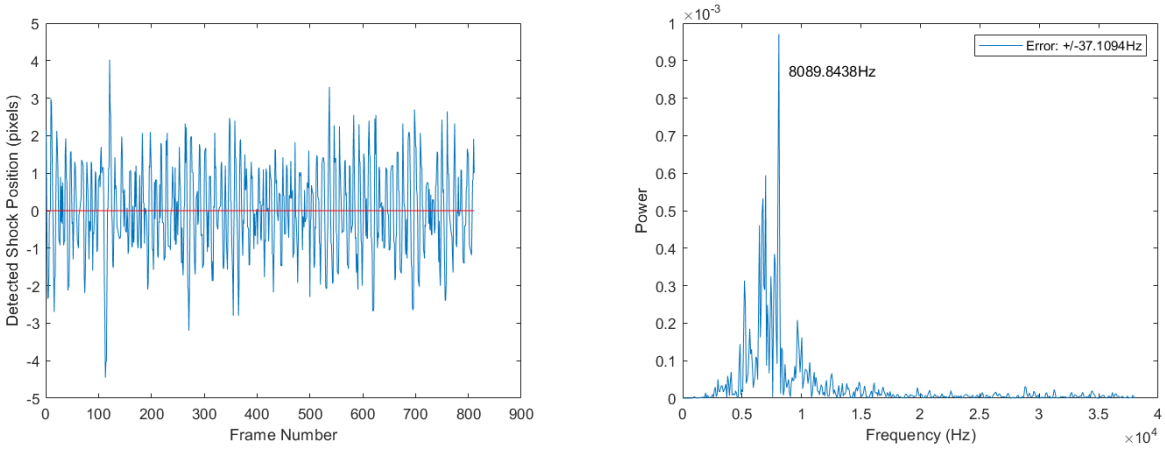

(a) (b)

Figure 6.2: (a) Tracked shock position for the unsteady 1/4" retronozzle case. (b) Frequency spectrum for the unsteady 1/4" retronozzle case.

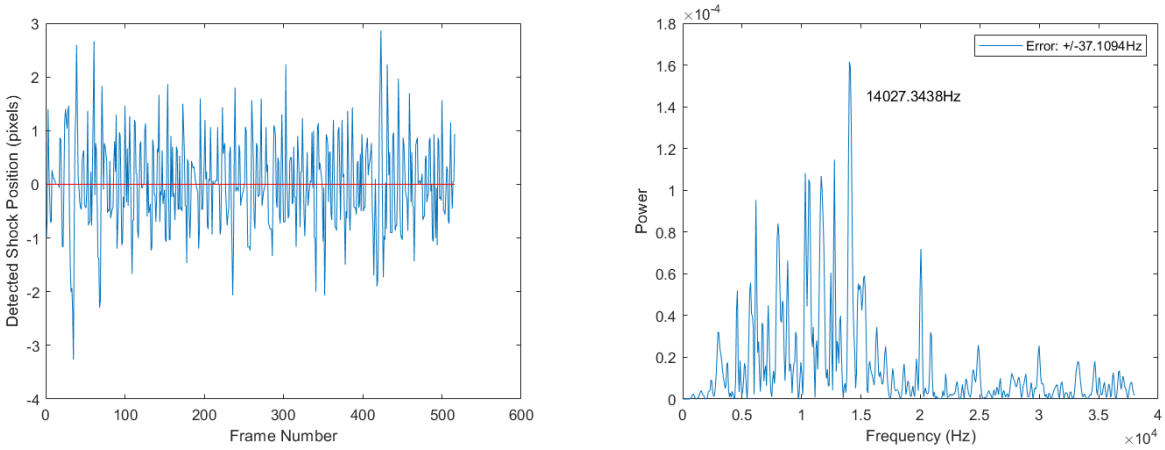

(a) (b)

Figure 6.3: (a) Tracked shock position for the unsteady 1/8" retronozzle case. (b) Frequency spectrum for the unsteady 1/8" retronozzle case.

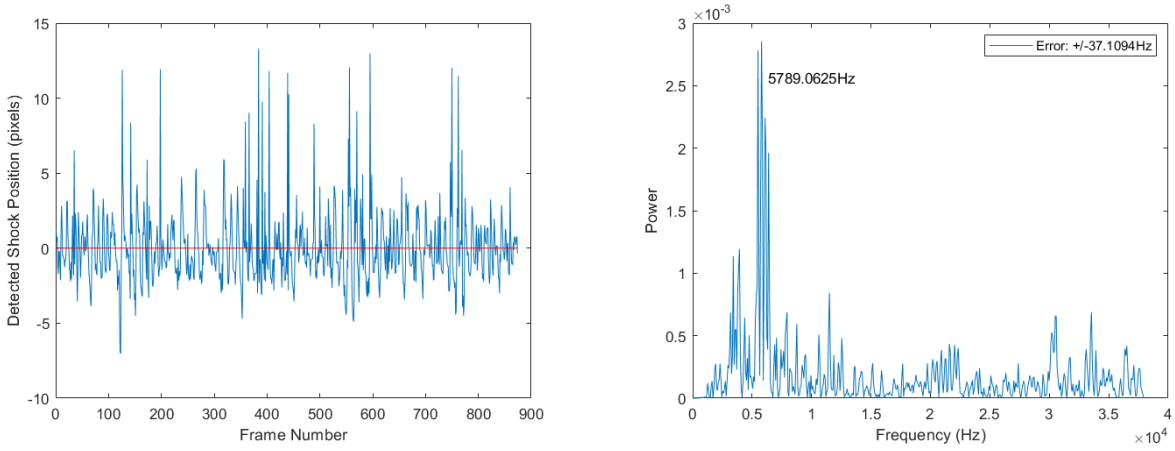

(a) (b)

Figure 6.4: (a) Tracked shock position for the unsteady 1/8" retronozzle with 1/4" forebody case. (b) Frequency spectrum for the unsteady 1/8" retronozzle with 1/4" forebody case.

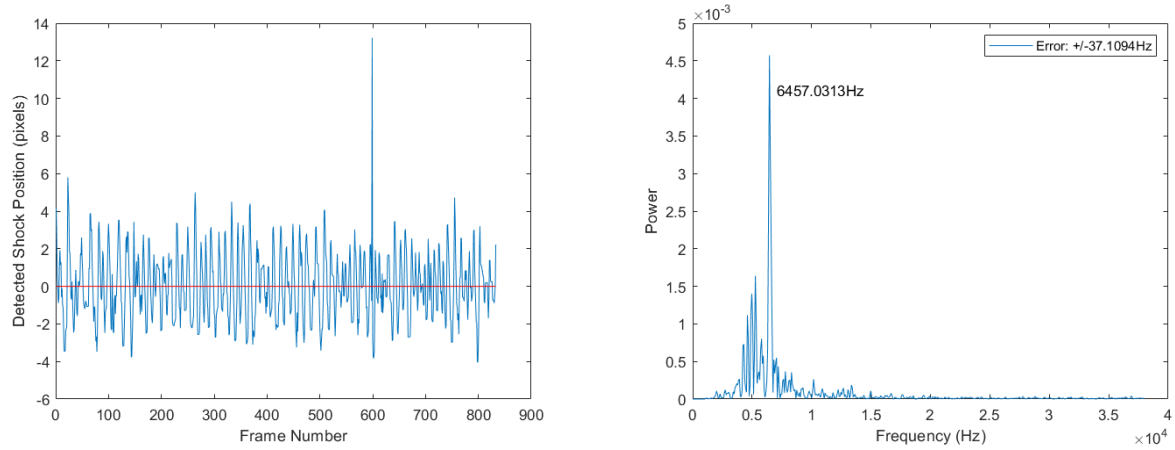

(a) (b)

Figure 6.5: (a) Tracked shock position for the unsteady 1/8" retronozzle with 3/8" forebody case. (b) Frequency spectrum for the unsteady 1/8" retronozzle with 3/8" forebody case.

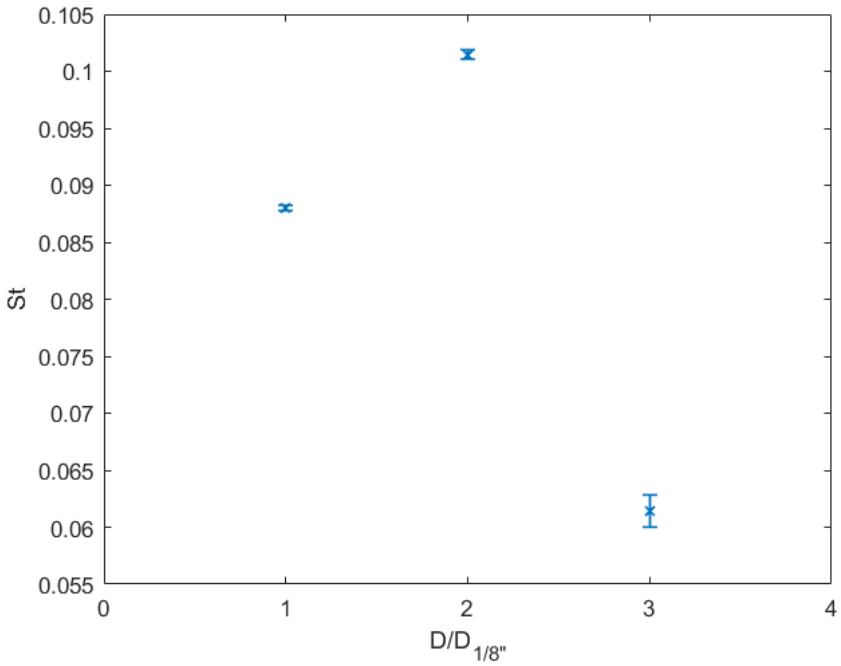

Figure 6.6: The Strouhal numbers for each of the simple nozzles tested at unity pressure.

References

[1] Miller, D. W., "2015 NASA Technology Roadmaps TA 9: Entry, Descent, and Landing," Tech. rep., National Aeronautics and Space Administration, Office of the Chief Technologist, NASA Headquarters, Washington, D.C., 2015.

[2] Joshua Buck, D.C. Agle, K. N., "NASA's LDSD Project Completes Second Experimental Test Flight," Digital Press Release, June 2015.

[3] Fagin, M., *Payload mass improvements of supersonic retropropulsive flight for human class missions to Mars*, Master's thesis, Purdue University, 2015.

[4] Romeo, D. J., "Exploratory investigation of the effect of a forward-facing jet on the bow shock of a blunt body in a Mach number 6 free stream," *NASA TN*, 1963, pp. TN–D.

[5] Berry, S., Rhode, M., Edquist, K., and Player, C., "Supersonic Retropropulsion Experimental Results from the NASA Langley Unitary Plan Wind Tunnel," *42nd AIAA Thermophysics Conference*, 2011, p. 3489.

[6] Berry, S. A., Rhode, M. N., and Edquist, K. T., "Supersonic Retropropulsion Experimental Results from NASA Ames 9× 7 Foot Supersonic Wind Tunnel," *Journal of Spacecraft and Rockets*, Vol. 51, No. 3, 2014, pp. 724–734.

[7] Daso, E. O., Pritchett, V. E., Wang, T.-S., Ota, D. K., Blankson, I. M., and Auslender, A. H., "Dynamics of shock dispersion and interactions in supersonic freestreams with counterflowing jets," *AIAA journal*, Vol. 47, No. 6, 2009, pp. 1313–1326.

[8] Tan, Y. M., *Influence of Pressure on Supersonic Retropropulsion Flow Field at Mach 2*, Master's thesis, University of Washington, 2018.

[9] McGhee, R., "Effects of a Retronozzle Located at the Apex of a 140 deg Blunt Cone at Mach Numbers of 3.00, 4.50, and 6.00," 1971.

[10] Korzun, A. M., *Aerodynamic and performance characterization of supersonic retropropulsion for application to planetary entry and descent*, Ph.D. thesis, Georgia Institute of Technology, 2012.

[11] Finley, P., "The flow of a jet from a body opposing a supersonic free stream," *Journal of Fluid Mechanics*, Vol. 26, No. 2, 1966, pp. 337–368.

[12] Pai, S.-I., *Fluid dynamics of jets*, van Nostrand, 1954.

[13] Pindzola, M., "Jet simulation in ground test facilities," Tech. rep., ADVISORY GROUP FOR AERONAUTICAL RESEARCH AND DEVELOPMENT PARIS (FRANCE), 1963.

[14] Venkatachari, B. S., Cheng, G., Chang, C.-L., Zichettello, B., and Bilyeu, D. L., "Long Penetration Mode Counterflowing Jets for Supersonic Slender Configurations—A Numerical Study," *31st AIAA Applied Aerodynamics Conference*, 2013, p. 2662.

[15] Wang, C.-M., *Transient Flow Analysis of a Supersonic Ludwieg-Tube Wind Tunnel*, Master's thesis, University of Texas, Arlington, 1989.

[16] Yang, X., *Influence of Jet Pressure on Multi-nozzle Supersonic Retropropulsion Flowfields*, Master's thesis, University of Washington, 2019.

[17] Lincoln, D., *Development and Characterization of an LED-Based Light Source for High-Speed Schlieren Imaging*, Master's thesis, University of Calgary, 2016.

[18] Bakhtian, N. and Aftosmis, M., "Analysis of Inviscid Simulations for the Study of Supersonic Retropropulsion," *29th AIAA Applied Aerodynamics Conference*, 2011, p. 3194.

[19] Sobey, I. J., "Oscillatory flows at intermediate Strouhal number in asymmetric channels," *Journal of Fluid Mechanics*, Vol. 125, 1982, pp. 359–373.

[20] Korzun, A. M. and Braun, R. D., "Performance characterization of supersonic retropropulsion for high-mass mars entry systems," *Journal of Spacecraft and Rockets*, Vol. 47, No. 5, 2010, pp. 836–848.

[21] Korzun, A., Braun, R., and Cruz, J., "Survey of supersonic retropropulsion technology for mars entry, descent, and landing," *Journal of Spacecraft and Rockets*, Vol. 46, No. 5, 2009, pp. 929–937.

[22] Korzun, A., Cordell, Jr, C., and Braun, R., "Comparison of inviscid and viscous aerodynamic predictions of supersonic retropropulsion flowfields," *10th AIAA/ASME Joint Thermophysics and Heat Transfer Conference*, 2010, p. 5048.